buildings

MDPI

Article

Effect of Na_2CO_3 Replacement Quantity and Activator Modulus on Static Mechanical and Environmental Behaviours of Alkali-Activated-Strain-Hardening-Ultra-High-Performance Concrete

Ke-Xian Zhuo [1], Gai Chen [1], Rui-Hao Luo [1], Yi-Wu Chen [2], De-Hui Li [3] and Jia-Xiang Lin [1,*]

[1] School of Civil and Transportation Engineering, Guangdong University of Technology, Guangzhou 510006, China; kexzhuo@163.com (K.-X.Z.); 13113976160@163.com (G.C.); luoryann@outlook.com (R.-H.L.)
[2] Guangdong Jialin Construction Co., Ltd., Maoming 525000, China; cosonz@163.com
[3] Guangdong Shenghong Construction Engineering Co., Ltd., Dongguan 523808, China; z583210701@126.com
* Correspondence: jxiang.lin@gdut.edu.cn; Tel.: +86-203-9322-538

Abstract: The application of alkali-activated concrete (AAC) shows promise in reducing carbon emissions within the construction industry. However, the pursuit of enhanced performance of AAC has led to a notable increase in carbon emissions, with alkali activators identified as the primary contributors. In an effort to mitigate carbon emissions, this study introduces Na_2CO_3 as a supplementary activator, partially replacing sodium silicate. The objective is to develop a low-carbon alkali-activated-strain-hardening-ultra-high-performance concrete (ASUHPC). The experimental investigation explores the impact of varying levels of Na_2CO_3 replacement quantity (0, 0.75 Na_2O%, and 1.5 Na_2O%) and activator modulus (1.35, 1.5, and 1.65) on the fresh and hardened properties of ASUHPC. The augmentation of Na_2CO_3 replacement quantity and activator modulus are observed to extend the setting time of the paste, indicating an increase in the modulus of the activator and Na_2CO_3 replacement quantity would delay the setting time. While the use of Na_2CO_3 intensifies clustering in the fresh paste, it optimizes particle grading, resulting in higher compressive strength of ASUHPC. The tensile crack width of ASUHPC conforms to the Weibull distribution. ASUHPC with a Na_2CO_3 replacement quantity of 0.75 Na_2O% exhibits superior crack control capabilities, maintaining a mean crack width during tension below 65.78 μm. The tensile properties of ASUHPC exhibit improvement with increasing Na_2CO_3 replacement quantity and activator modulus, achieving a tensile strength exceeding 9 MPa; otherwise, increasing the activator modulus to 1.5 improves the deformation capacity, reaching 8.58%. Moreover, it is observed that incorporating Na_2CO_3 as a supplementary activator reduces the carbon emissions of ASUHPC. After considering the tensile performance indicators, increasing the activator modulus can significantly improve environmental performance. The outcomes of this study establish a theoretical foundation for the design of low-carbon, high-performance-alkali-activated-strain-hardening-ultra--high-performance concrete.

Keywords: alkali-activated; carbon emission; cracking characteristics; geopolymer; ultra-high performance

Citation: Zhuo, K.-X.; Chen, G.; Luo, R.-H.; Chen, Y.-W.; Li, D.-H.; Lin, J.-X. Effect of Na_2CO_3 Replacement Quantity and Activator Modulus on Static Mechanical and Environmental Behaviours of Alkali-Activated-Strain-Hardening-Ultra-High-Performance Concrete. *Buildings* **2024**, *14*, 681. https://doi.org/10.3390/buildings14030681

Academic Editor: Dan Bompa

Received: 7 February 2024
Revised: 26 February 2024
Accepted: 1 March 2024
Published: 4 March 2024

1. Introduction

With the progress of societal development, engineering structural design has placed higher demands on aspects such as lightweight construction, service life, and space utilization. Consequently, the requirements for mechanical performance and durability of construction materials have continued to increase [1–3]. To meet these societal needs,

some typical high-performance concrete materials have been proposed, in the form of ultra-high-performance concrete (UHPC) and engineered cementitious composites (ECC).

UHPC is known for its extremely high compressive strength (≥120 MPa), durability, and high toughness [4–6]. However, it also has limitations, in terms of deformation and crack control [7,8]. When subjected to cracked conditions, the internal steel fibers in UHPC are prone to corrosion from aggressive media, which can weaken its mechanical properties. On the other hand, ECC is a highly ductile fiber-reinforced concrete with excellent deformability and crack control capabilities, which typically exhibits tensile strains of over 3% [9–11], and can effectively enhance the durability and seismic performance of structural elements [12,13]. Researchers have conducted extensive studies to develop high-performance concrete that combines both ultra-high strength and exceptional tensile properties [14–17]. Kunieda et al. [14] developed a high-performance strain-hardening cementitious composite (UHP-SHCC), which combines the strength of UHPC with the tensile characteristics of ECC. This remarkable material demonstrates strain-hardening behavior and multiple cracking characteristics. Yu et al. [18] further enhanced the mechanical properties of UHP-SHCC, and proposed a ultra-high-performance engineered cementitious composite (UHP-ECC) with impressive compressive strength, tensile strength, and tensile strain values of 121.5 MPa, 17.4 MPa, and 8.7%, respectively. The introduction of UHP-ECC provides a material foundation for designing more daring structures and enhances the seismic performance and safety reserve of building structures [17]. The production of high-performance concrete such as UHPC and ECC requires a significant amount of cement. However, the cement industry is currently recognized as one of the major sources of carbon emissions, with each ton of cement production resulting in 0.66–0.82 tons of CO_2 emissions [19]. Therefore, it is crucial to find greener alternatives to cement that can be used as binder materials to improve the sustainability of high-performance concrete.

In recent years, geopolymer or alkali-activated binder has received significant attention for its potential to enhance the sustainability of high-performance concrete materials by reducing carbon emissions [20,21]. Alkali-activated materials (AAM) are three-dimensional inorganic structures obtained by reacting alkaline/acidic activators with silica-alumina-rich raw materials. The raw materials used for AAM have a low carbon footprint and are widely available, including materials such as kaolin, feldspar, and other silicate-aluminate materials, as well as industrial solid wastes like slag, fly ash, and others. Alkali-activated concrete (AAC) has been shown to have carbon emissions ranging from 9% to 80% lower than cement-based concrete [22,23]. Numerous studies have demonstrated the potential of alkali-activated binder as a substitute for cement in the production of high-performance concrete [24–29]. Ambily et al. [24] proposed ultra-high-performance geopolymer concrete (UHPGC) with compressive strength exceeding 120 MPa under ambient curing conditions. Lao et al. [30] developed UHPGC with tensile strain-hardening behavior, achieving tensile strain capacity ranging from 0.35% to 0.55% and an impressive compressive strength of 222 MPa. Ohno et al. [31] utilized PVA fibers to create geopolymer composites with a tensile strain exceeding 4%, and an average crack width of the material at 4.5% strain that was only 45 μm. These research findings highlight the wide-ranging applications of alkali-activated binder in the field of high-performance concrete.

Currently, high-performance alkali-activated concrete commonly utilizes NaOH-Na_2SiO_3 activator, which have high activation efficiency. The sodium silicate modulus (molar ratios of SiO_2/Na_2O) significantly affects the mechanical and workability properties of AAC [28,32,33]. Li et al. [33], using the Taguchi method, investigated the influence of different mixture proportional factors on the performance of slag-based geopolymer concrete and found an optimal modulus that resulted in good flowability and compressive strength of AAC. Mousavinejad et al. [34] studied the effect of modulus on the fracture performance of ultra-high performance geopolymer concrete (UHPGC) and found that the fracture toughness of UHPGC increased with an increase in the ratio. Although AAC is considered a sustainable alternative to cement concrete, the significant increase in carbon emissions resulting from the enhanced performance of geopolymer concrete cannot

be ignored [35]. The carbon emissions from AAC activated with NaOH-Na_2SiO_3 are primarily generated by alkali activators and account for up to 80% of emissions [36,37]. Therefore, using alkali activators with lower carbon emissions is an effective approach to reduce the carbon footprint of high-performance alkali-activated concrete.

To further reduce carbon emissions in AAC, researchers have started exploring the use of alkalis and salts (such as $Ca(OH)_2$, Na_2CO_3, $CaCO_3$, and $NaAlO_2$) with lower alkalinity and carbon emissions as activators or supplementary activators in AAC production [38–43]. Ma et al. [42] utilized Na_2CO_3 as a partial replacement for sodium silicate to prepare AAC based on slag and slag-fly ash, and found that the use of Na_2CO_3 effectively reduced CO_2 emissions. Bian et al. [44] developed ferronickel slag-based geopolymer using Na_2CO_3 and $Ca(OH)_2$ as binding activators, achieving a compressive strength of 48.3 MPa. Díaz et al. [45] prepared single component geopolymer paste using CaO-Na_2CO_3 as an activator and observed a carbon emission reduction of 49–58%, compared to cement. These studies demonstrate that the use of activators or supplementary activators with lower alkalinity and carbon emissions can effectively reduce the carbon footprint of AAC, providing a new pathway for achieving low-carbon and environmentally friendly building materials.

However, the application of Na_2CO_3 as an activator in high-ductility alkali-activated concrete is currently lacking, and the impact of the mechanisms of sodium silicate modulus and Na_2CO_3 on the tensile properties of high-ductility concrete remain unclear. In this study, we further develop existing high-performance-alkali-activated concrete and propose an alkali-activated-strain-hardening-ultra-high-performance concrete (ASUHPC) that combines ultra-high compressive strength with excellent tensile performance. Na_2CO_3 is used as a supplementary activator, and the influence of Na_2CO_3 replacement level and sodium silicate modulus on the workability and mechanical properties of ASUHPC is investigated. The environmental performance of ASUHPC is also evaluated in this study. The aim of this research is to provide alternative solutions for reducing carbon emissions in alkali-activated-strain-hardening-ultra-high-performance concrete and to propose a design approach for low carbon and environmentally friendly ASUHPC.

2. Test Program

2.1. Materials

Table 1 presents the mix proportions of ASUHPC used in this study. The composition of ASUHPC mainly includes precursors, activators, fine aggregates, fibers, and additives. The precursors consist of S105-grade ground granulated blast furnace slag (GGBS, GB/T 18046 [46]), Class F fly ash (FA, ASTM C618 [47]), and silica fume (SF). The activators consist of sodium hydroxide, sodium silicate solution, and sodium carbonate. The sodium silicate solution has a modulus of 2.25, with a composition of Na_2O: SiO_2: H_2O = 29.99 wt%: 13.75 wt%: 56.26 wt%. The fine aggregates are quartz sand (QS, 2.3 g/cm^3), which includes fine sand (FS, 40–200 μm) and middle sand (MS, 200–700 μm). The additives include $BaCl_2$, defoamer, and sodium lignosulfonate (SLS). $BaCl_2$ is used to extend the setting time of alkali-activated binder, and can react with water glass to form a dense coating layer on the surface of slag particles, thereby preventing direct contact between slag powder and water glass and achieving a certain retarding effect [29]. The defoamer is used to reduce large size defects in the alkali-activated matrix, and SLS is used to improve the workability of the alkali-activated matrix in an alkaline environment [48]. Alkali-activated binder with a higher content of slag exhibit a denser structure and a larger proportion of pores below 50 nm, resulting in a higher tendency for shrinkage cracking [49]. Therefore, in this study, cost-effective Nano $CaCO_3$ (NC, 10–100 nm, 2.8 g/cm^3) was used to fill the pores and reduce matrix shrinkage cracking. The fibers used are ultra-high molecular weight polyethylene fibers (PE), and their physical properties are provided in Table 2. Table 3 presents the chemical composition of the binder materials, while Figure 1 illustrates the microstructure of GGBS, FA, and SF. Figure 2 illustrates the particle size distribution of the solid

materials, which was obtained by using a particle size analyzer (Mastersizer 3000, Malvern, UK).

Table 1. Mix proportions of ASUHPC (weight ratio).

Mix IDs	GGBS	FA	SF	MS	FS	$BaCl_2$	Defoamer	SLS	NC	W/B [a]	N/B [b]	Activator Modulus	Na_2CO_3 (Na_2O%)	PE Fiber
M1-N1												1.35	0	
M1-N2												1.35	0.75	
M1-N3	0.71	0.21	0.08	0.05	0.30	0.01	0.001	0.005	0.02	0.3	7%	1.35	1.5	2 vol%
M2-N1												1.50	0	
M3-N1												1.65	0	

[a] W/B ratio represents the mass ratio of water to binder materials, $W/B=(m_w(\text{Activator})+m_w(\text{Extra water}))/m_{\text{Binder}}$; [b] N/B ratio represents the ratio of equivalent Na_2O mass to the mass of binder materials; The dosage of Na_2CO_3 is expressed in terms of equivalent Na_2O mass, indicated as Na_2O% in the composition [33].

Table 2. Physical and mechanical properties of PE fiber.

Diameter (μm)	Length (mm)	Strength (MPa)	Elastic Modules (GPa)	Density (g/cm^3)
24	18	3000	116	0.97

Table 3. Chemical composition of GGBS, FA and SF.

Oxide	GGBS	FA	SF
		wt%	
CaO	34	4.01	/
SiO_2	34.5	53.97	94.73
Al_2O_3	17.7	31.15	/
SO_3	1.64	2.2	0.2
Fe_2O_3	1.03	4.16	/
MgO	6.01	1.01	/
TiO_2	/	1.13	/
Others	5.12	2.37	5.07
LOI (%)	0.84	4.6	1.5
density (g/cm^3)	3.1	2.3	2.25
D_{10} (μm)	1.65	3.55	0.10
D_{50} (μm)	8.68	14.46	0.14
D_{90} (μm)	24.09	58.88	0.35

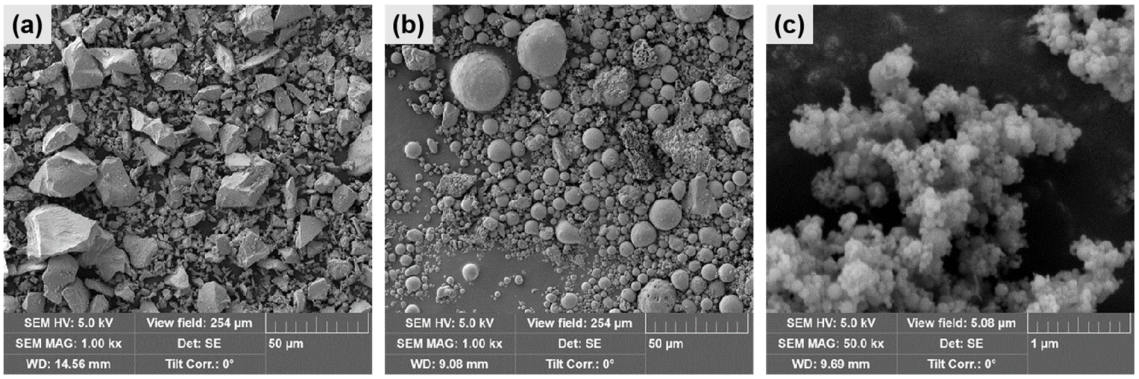

Figure 1. SEM photographs of precursors. (**a**) GGBS; (**b**) FA; (**c**) SF.

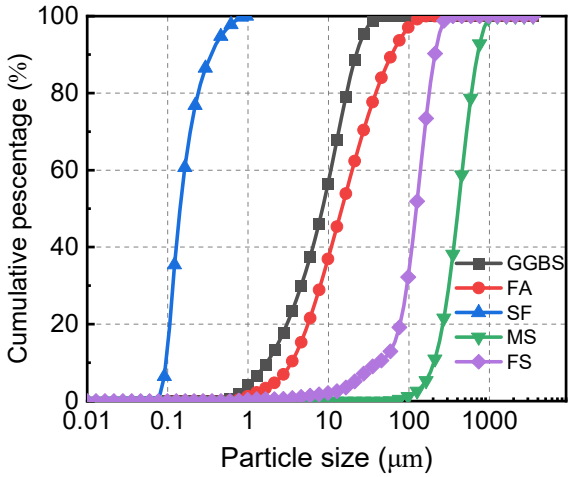

Figure 2. Particle size distribution of solid materials.

2.2. Specimens Preparation

The mechanical performance testing of this study includes compressive tests and axial tensile tests, conducted using cubic specimens and dumbbell-shaped specimens, respectively. The dimensions of the cubic specimens are 50 × 50 × 50 mm^3, while the dimensions of the dumbbell-shaped specimens are shown in Figure 3. The preparation of ASUHPC specimens involves initial preparation of the activator, mixing procedures, casting, and subsequent curing, as illustrated in Figure 4:

(1) Prepare the activator by mixing cooled NaOH solution (14 mol/L) with Na_2SiO_3 solution to achieve the desired modulus. Cool the solution for 24 h and then add a sodium carbonate solution (25 wt%) to the mixture. Seal it. Alkaline activators with high temperatures will accelerate the geological polymerization and hydration reactions of cementitious materials, leading to the occurrence of flash setting in composite materials.

(2) Add the precursor to a mixer and dry mix at 75 r/min for 3 min. Add quartz sand and continue dry mixing for another 3 min. Mix the activator with extra water and add it to the mixer, and follow with high-speed (165 r/min) mixing with water reducer and Nano $CaCO_3$ for 2 min. Switch to low speed and add PE fiber within 3 min. Mix at low speed for 2 min to ensure uniform dispersion.

(3) Pour the mixture into molds, vibrate to remove air bubbles, and achieve a smooth surface. Cover with a moisture-retaining film and cure in the laboratory for 1 day. Demold the specimens and subject them to water curing at room temperature. After 28 days of curing, perform mechanical performance tests.

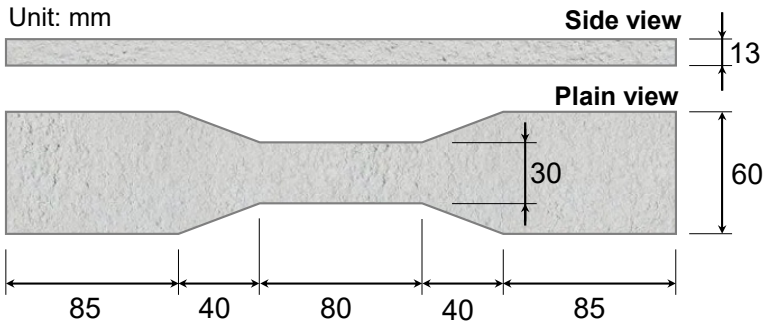

Figure 3. Dimension of dumbbell specimen.

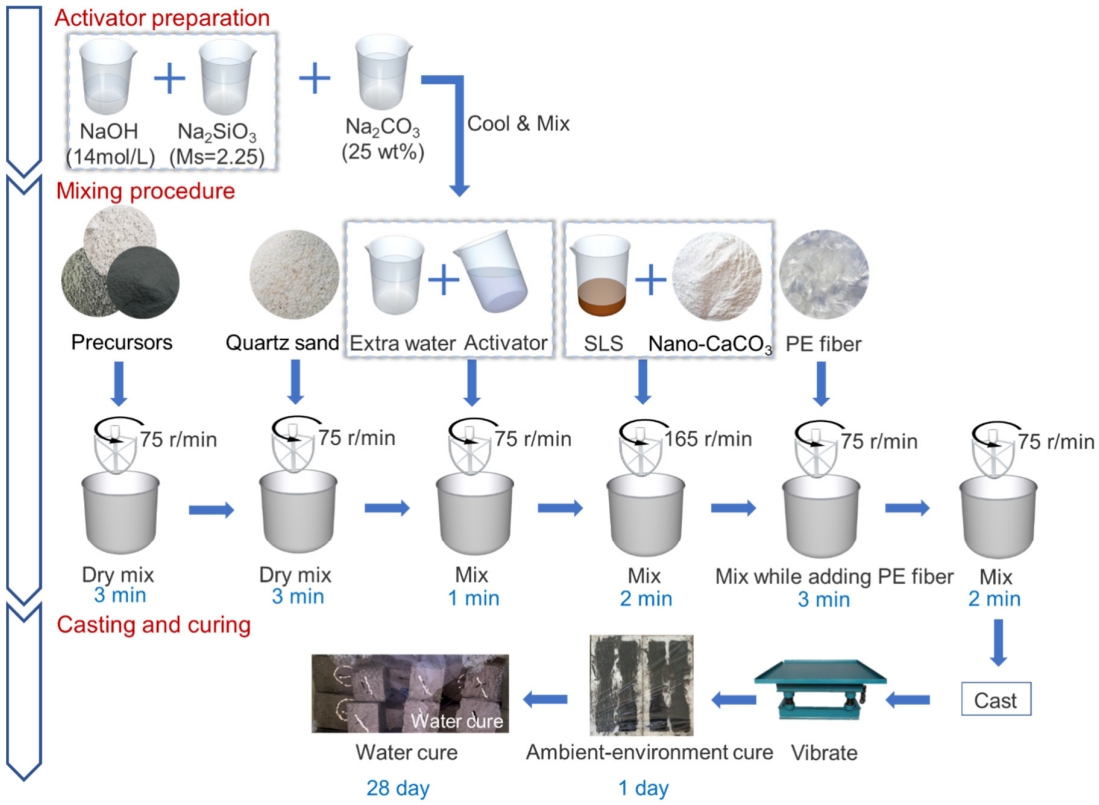

Figure 4. The specimen preparation method of ASUHPC.

2.3. Test Method

This study conducted experiments related to the workability, mechanical properties, and microstructure of ASUHPC, including tests of setting time, the particle size distribution of fresh paste and compressive and tensile strength. Microscopic analysis using X-ray diffraction (XRD) and scanning electron microscopy (SEM) was also undertaken.

2.3.1. Setting Time

The setting time of alkali-activated paste was determined using a Vicat apparatus according to the standard GB/T 1346 [50]. The laboratory environment during the test had a temperature of 24.5 °C and a relative humidity of 89%. The preparation of the paste excluded some of the raw materials (quartz sand, fibers, SLS, and nano calcium carbonate) and followed the procedure shown in Figure 5. The total mixing time after adding the activator was 8 min.

2.3.2. Size Distribution of Fresh Alkali-Activated Pastes

The test setup for the particle size distribution of the fresh pastes followed the methodology described in a previous study by Zhang et al. [51]. The fresh pastes (consistent with the setting time test) were immediately taken out and added to an adequate amount of distilled water to create a suspension with a pH of 7, effectively stopping the reaction of the mixture. After 3 days, a particle size analyzer (Mastersizer 3000) was used to measure the particle size distribution of the solid particles in the suspension (Figure 5a). The materials used in the preparation are all non-hydraulic materials, and storing them in a pH = 7 environment for 3 days will not affect the original particle size distribution of the materials in the fresh slurry.

2.3.3. Mechanical Behaviors

The compressive test was conducted in accordance with ASTM C109/C109M [52], using a load-controlled method with a loading rate of 1.75 kN/s. The tensile test was conducted according to the JSCE (2008) [53]. Two linear variable differential transformers (LVDTs) were placed on both sides of the specimen using fixtures to measure deformation within the gauge zone (Figure 5c). The tensile test was performed using a displacement-control method at a rate of 0.5 mm/min. Additionally, a camera with an effective pixel count of 24.2 million (Sony A7 III) was used to capture images of the crack characteristics within the image collection zone during the tensile process. The images were subjected to binarization processing, and crack information, such as crack number, crack width, and crack distribution, was extracted and analyzed statistically.

2.3.4. X-ray Diffraction (XRD)

The hardened paste obtained from the setting time test after 14 days of curing was ground to obtain dry powder for mineralogical characterization using X-ray diffraction (XRD, Rigaku Miniflex 600, Tokyo, Japan) with Cu Kα radiation. The XRD analysis was performed in the range of 10–70° 2θ, with a scanning speed of 2°/min.

2.3.5. Scanning Electron Microscopy (SEM)

The samples were analyzed for microstructure using a scanning electron microscope (SEM, Hitachi S-3400N, Tokyo, Japan) at an accelerating voltage of 15 keV. The test specimens included: (1) Blocks with fibers on the fracture surface of the tensile specimens, used to analyze the failure mode of fibers in ASUHPC; (2) Blocks obtained from the setting time test after 14 days of curing, used to analyze the microstructure of the alkali-activated paste.

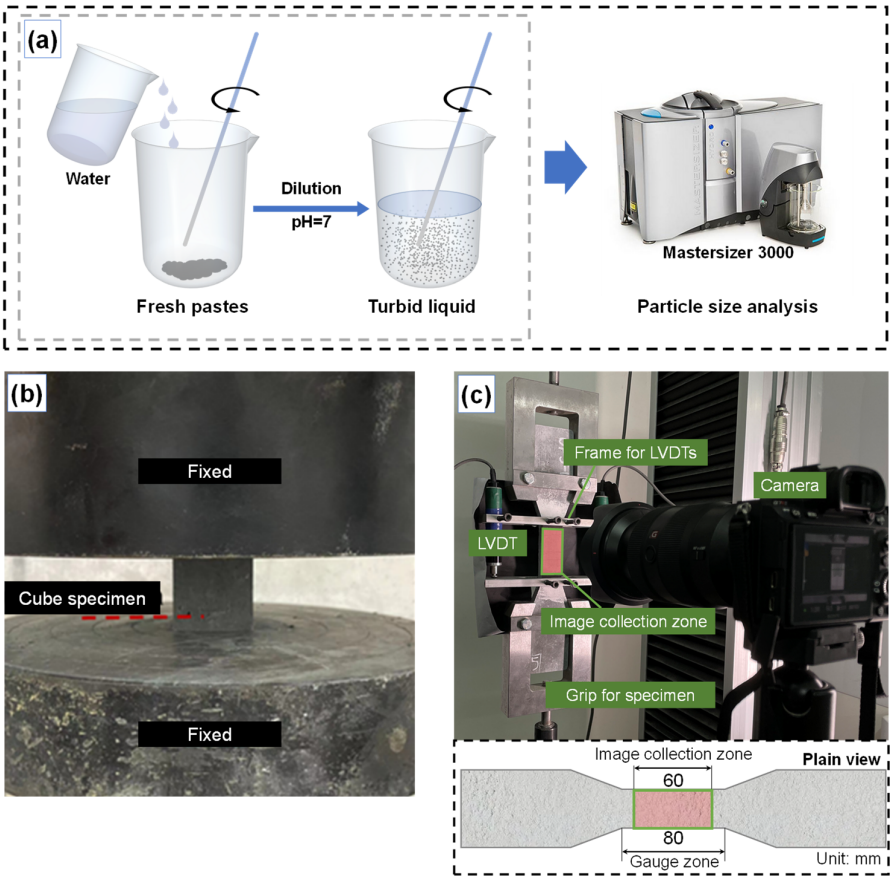

Figure 5. Test setup. (**a**) Particle size analysis of fresh pastes; (**b**) Compressive test; (**c**) Tensile test.

3. Results

3.1. Effect of Replacement Quantity of Na_2CO_3 and Modulus of Activator on Fresh Behavior

3.1.1. Setting Time

Figure 6 illustrates the setting time of fresh alkali-activated paste for different replacement quantities of Na_2CO_3 and different activator modulus. It can be observed in Figure 6 that as the replacement quantity of Na_2CO_3 increases, both the initial and final setting times of the alkali-activated paste are prolonged. When the replacement quantity of Na_2CO_3 is 1.5 Na_2O%, the M1–N3 exhibits an initial setting time of 47 min and a final setting time of 57 min, representing an increase of 56.7% and 42.5% respectively, compared to the M1–N1. This could be attributed to the fact that the replacement of NaOH-Na_2SiO_3 with Na_2CO_3 reduces the pH value of the alkali-activated paste liquid phase, which slows down the leaching of elements such as Ca, Si, Al from the precursors. Additionally, the reduction of $[SiO_4]^{4-}$ also delays the formation of the three-dimensional network structure of the geopolymer gel [42]. Furthermore, as observed in Figure 6, increasing the activator modulus also effectively delays the setting of the paste. The M3–N1 sample with a modulus of 1.65 exhibits initial and final setting times of 57 min and 65 min, respectively. However, although increasing the modulus prolongs the initial setting time, it also reduces the time interval between the final and initial setting times: this could be attributed to the fact that increasing the modulus leads to an increase in the content of $[SiO_4]^{4-}$, which results in the rapid binding of leached cations to form a three-dimensional network gel, consequently reducing the time interval between initial and final setting times.

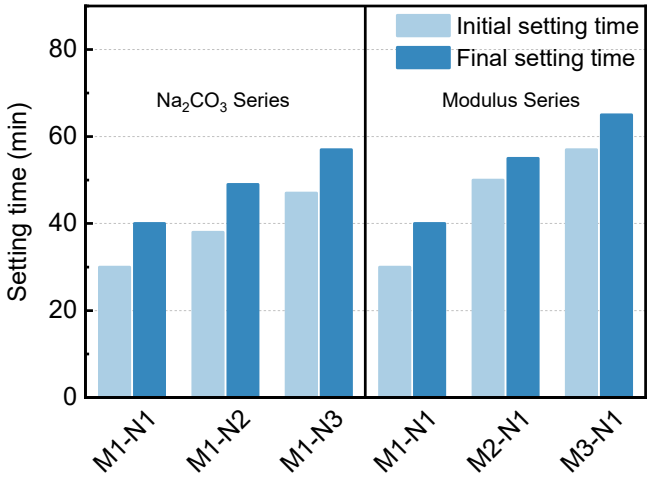

Figure 6. Setting time of ASUHPC with different replacement quantities of Na_2CO_3 and modulus of activator.

3.1.2. Size Distribution of Fresh Alkali-Activated Pastes

Figure 7 shows the particle size distribution curves of fresh alkali-activated paste for different replacement quantities of Na_2CO_3 and activator modulus. It can be observed that the Na_2CO_3 replacement quantities and activator modulus have a significant impact on the particle size distribution of fresh alkali-activated paste. D_{90}, D_{50}, and D_{10} represent the particle sizes corresponding to the cumulative percentage distribution reaching 90%, 50%, and 10%, respectively. With an increase in Na_2CO_3 replacement quantities, the median particle size (D_{50}) and D_{10} decrease, while D_{90} increases. This can be attributed to the use of Na_2CO_3, which lowers the alkalinity of the liquid phase and slows down the dissolution of active components and the formation of polymerization products, thereby increasing the proportion of smaller-sized particles. In addition, the presence of $[CO_3]^{2-}$ leads to the formation of low-density calcium carbonate precipitates in the fresh paste, resulting in an

increase in the proportion of larger particles. In Figure 7, it can be observed that when the activator modulus increases, the D_{50} value of the fresh alkali-activated paste significantly decreases. This is primarily due to the fact that a lower activator modulus promotes the dissolution of reactive silico-aluminates, facilitating their polymerization and attachment to the precursor particle surfaces, resulting in the formation of larger particles [51].

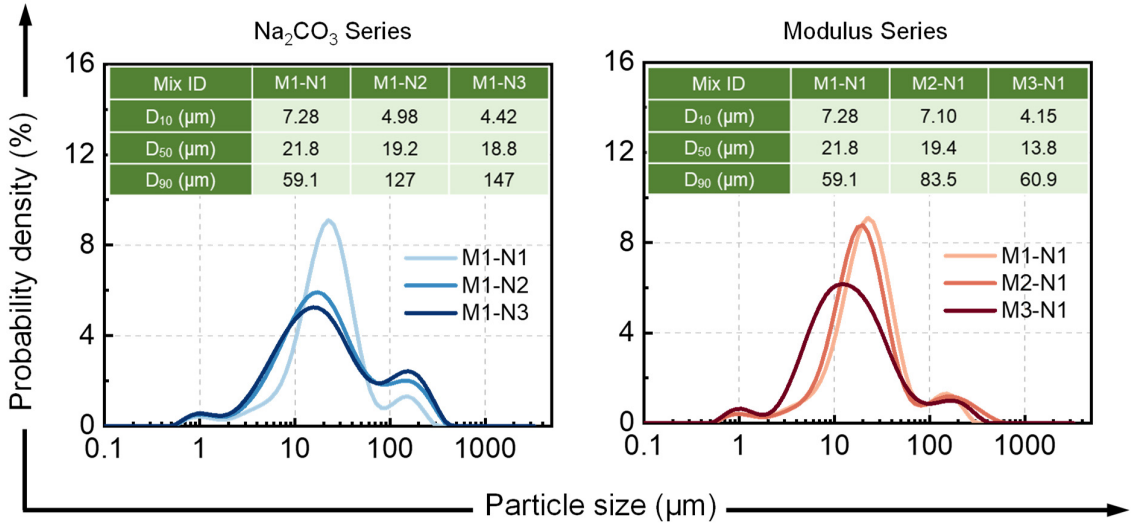

Figure 7. Particle size distribution curves of fresh alkali-activated paste with different Na_2CO_3 replacement quantities and activator modulus, along with parameters such as D_{90}, D_{50}, and D_{10}.

In Figure 7, the particle size distribution of fresh alkali-activated paste is shown for different replacement quantities of Na_2CO_3 and activator moduli. Figure 8a presents the cumulative particle size distribution curves of fresh alkali-activated paste for different Na_2CO_3 replacement quantities and activator modulus, compared to the modified A&A model curve. The modified A&A model is a classic model for maximum dry packing density of particles [54]. Its expression is as follows:

$$P_{tar}(D) = \frac{D^q - D_{\min}^q}{D_{\max}^q - D_{\min}^q} \quad (1)$$

where D represents the particle size, $P_{tar}(D)$ denotes the cumulative percentage of particles with a size smaller than D, D_{max}^q and $D_{\min}^q$ are the maximum and minimum particle sizes in the mixture, respectively; q is the distribution modulus, which is set to 0.23 in this study.

In order to investigate the effect of particle size distribution on the density variation of fresh alkali-activated paste, the residual sum of squares (RSS) between the cumulative particle distribution curve and the target curve was calculated using the least squares method, as shown in Figure 8b. A smaller RSS indicates the actual cumulative curve is closer to the ideal packing model, indicating a denser stacking [55]. In Figure 8b, it can be observed that increasing the Na_2CO_3 replacement quantity leads to a smaller RSS, indicating a denser particle packing. On the other hand, increasing the activator modulus has the opposite effect.

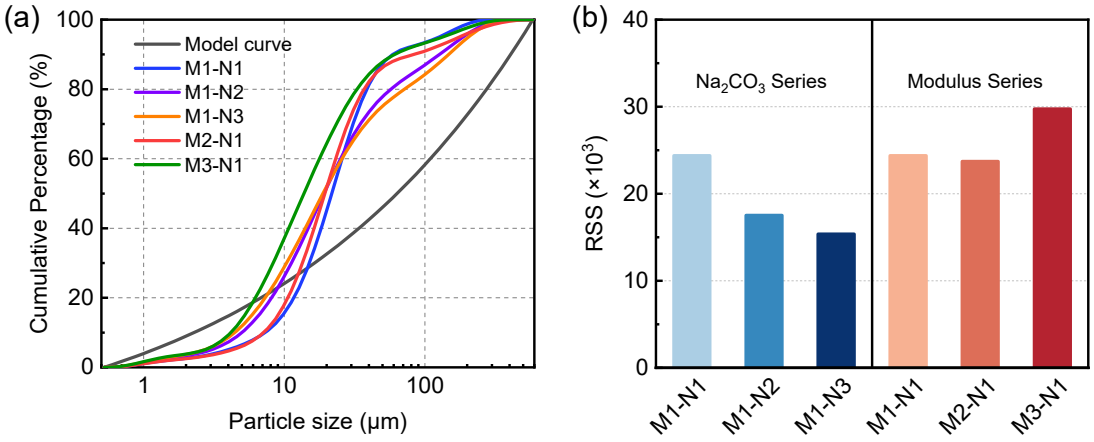

Figure 8. (**a**) The cumulative particle size distribution curves of fresh alkali-activated paste for different Na_2CO_3 replacement quantities and activator modulus, compared to the modified A&A model curve; (**b**) Comparison of the deviation (RSS) of the cumulative particle size distribution curve and the modified A&A model curve.

3.2. Effect of Replacement Quantity of Na_2CO_3 and Modulus of Activator on Compressive Strength

Figure 9 shows the compressive strength of ASUHPC for different Na_2CO_3 replacement quantities and activator modulus. Xu et al. [56] found that AAC achieves compressive strength in the range of 136.5–150.7 MPa when the Si/Al ratio is 2.4 and the Ca/(Si + Al) ratio is 0.33–0.38. In this study, the Si/Al ratio and Ca/(Si + Al) ratio are 2.27–2.46 and 0.34–0.36, respectively, and the compressive strength exceeds 120 MPa. It is worth noting that while the use of a certain Na_2CO_3 replacement quantity reduces the alkalinity of the activator, it actually increases the compressive strength of ASUHPC (from 122.9 MPa to 126.7 MPa), which is consistent with the findings of Lao et al. [57]. Indeed, the optimized Na_2CO_3 replacement quantity enhances the particle size distribution of fresh alkali-activated paste (as shown in Figure 8), resulting in improved density and, consequently, higher compressive strength of ASUHPC. Similarly, as observed in Figure 9, an increase in activator modulus leads to a decrease in the compressive strength of ASUHPC, which is attributed to the decrease in the density of fresh alkali-activated paste caused by the higher activator modulus [25].

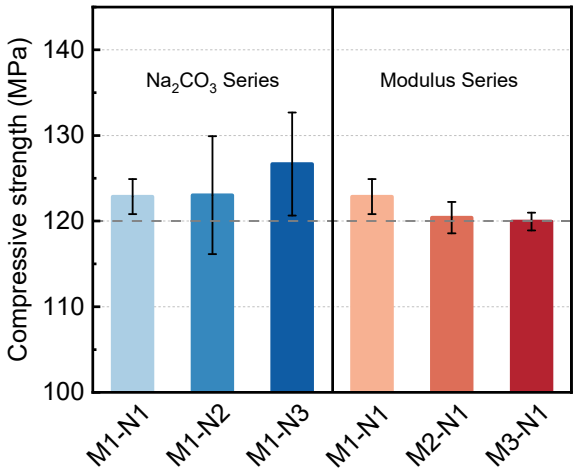

Figure 9. Compressive strength of ASUHPC for different Na_2CO_3 replacement quantities and activator modulus.

3.3. Effect of Replacement Quantity of Na_2CO_3 and Modulus of Activator on Tensile Behavior of ASUHPC

3.3.1. Cracking Behavior

To investigate the crack development of ASUHPC during the tensile test, a binarization-based digital image correlation method was employed to monitor and analyze the crack propagation process. Taking M1–N1 as an example, as shown in Figure 10, the images within the image collection zone were binarized during five strain stages (A, B, C, D, and U, with U representing the ultimate strain stage) of the tensile process. Cracks along the longitudinal axis of the specimen were identified, and the number, width, and distribution of the cracks were calculated.

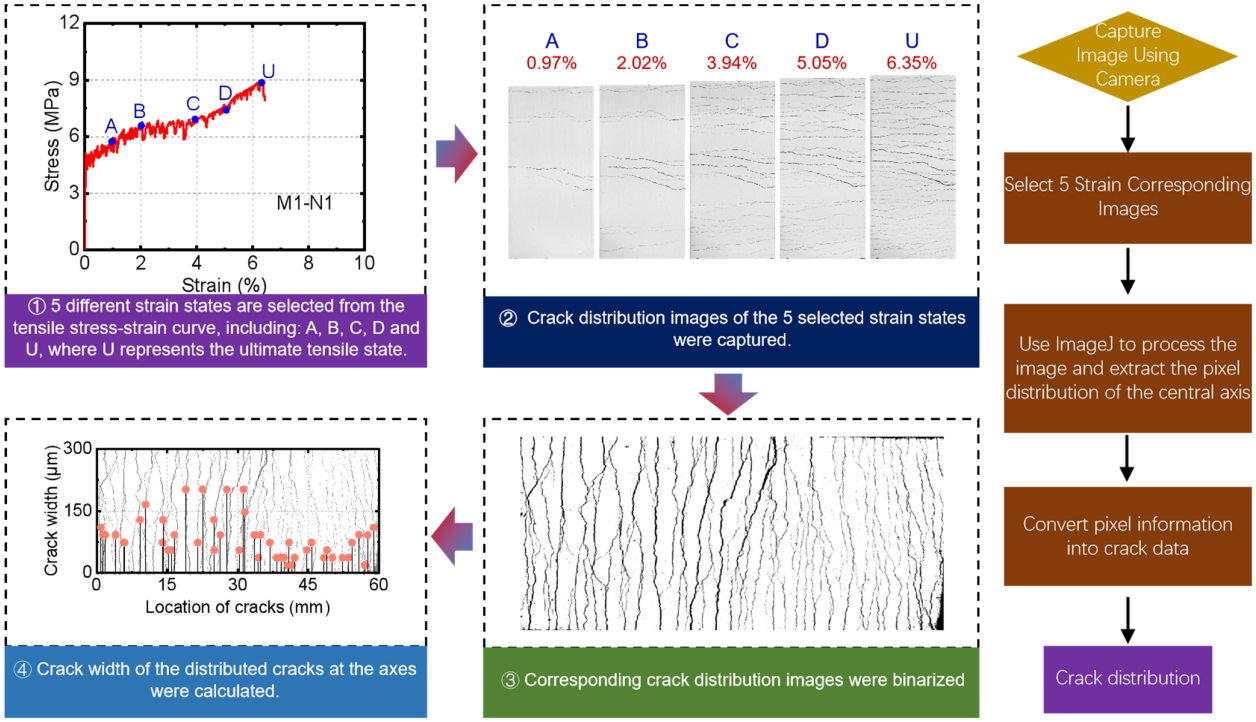

Figure 10. Processing and statistical procedure of crack initiation and propagation in tensile specimens using binarization-based digital image correlation method.

Figure 11 presents the crack width and distribution along the central axis of the specimens during each strain stage (A, B, C, D, and U), as well as the crack morphology at the ultimate stage. The left side of the image represents the distribution, number, and width of cracks in each strain stage. The horizontal scale of each grid in the image ranges from 0 to 400 μm, while the vertical scale corresponds to the length of the image collection zone. In the Na_2CO_3 series, it can be observed that at a Na_2CO_3 replacement quantity of 0.75 Na_2O%, there is an increase in the number of cracks, and the cracks appear more uniform and dense. When the Na_2CO_3 replacement quantity is further increased to 1.5 Na_2O%, the cracks initially exhibit smaller widths and a more uniform distribution. However, towards the end of the tensile process, the overall crack width increases, indicating a lower crack control capability, compared to M1–N1. In the Modulus series, it is evident that increasing the activator modulus weakens the crack control capability of ASUHPC, which is demonstrated by a significant reduction in the number of cracks and a substantial increase in crack width. Specifically, in the case of M2–N1, a crack with a width of 362 μm appears at the ultimate stage, highlighting the decreased crack control capability.

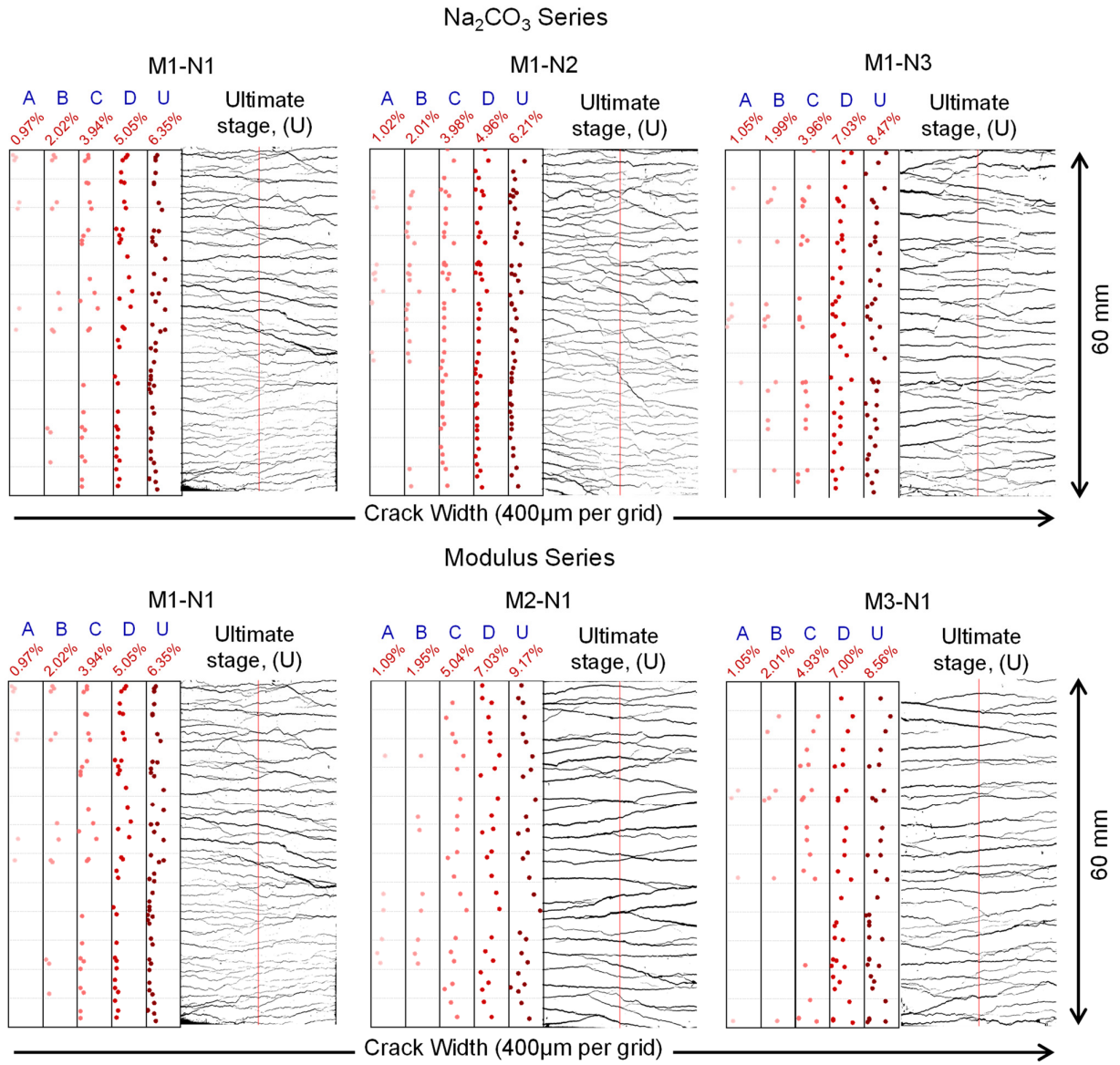

Figure 11. The binary images of crack distribution in ASUHPC at the ultimate stage, as well as the crack width and location distribution at the central axis of the specimen in each strain stage (A, B, C, D, and U), obtained through image processing techniques.

Statistical analysis of crack characteristics in ASUHPC was performed using the Weibull distribution. The cumulative distribution function (CDF) and probability density function (PDF) of the Weibull distribution are given by Equations (2) and (3), respectively. The mean and standard deviation of crack width calculated using the Weibull distribution are shown in Equations (4) and (5), respectively:

$$F(w) = 1 - \exp(-(w/\lambda)^k) \tag{2}$$

$$f(w) = (k/\lambda)(w/\lambda)^{(k-1)} \exp(-(w/\lambda)^k) \tag{3}$$

$$w_{mean} = \lambda\Gamma(1+1/k) \tag{4}$$

$$s_w = \lambda\sqrt{\Gamma(1+2/k) - \Gamma(1+1/k))^2} \quad (5)$$

where w represents the crack width obtained through image processing techniques, λ and k are the scale parameter and shape parameter of the Weibull distribution, respectively. The Weibull distribution provides a good fit to the distribution of crack widths in the tensile process of the specimens. The specific crack information is presented in Table 4.

Table 4. The crack characteristics and Weibull distribution parameters of ASUHPC during the tensile process for different Na_2CO_3 replacement quantities and activator modulus.

Mix IDs	Tensile Strain (%)	Number of Cracks	Tensile Strain (%)	Weibull Distribution				
				λ	k	R^2	w_{mean}	s_w
M1-N1	A: 0.97	7	A: 0.97	87.86	3.57	0.885	79.14	24.58
	B: 2.02	12	B: 2.02	122.11	2.96	0.938	108.98	40.06
	C: 3.94	26	C: 3.94	97.66	1.84	0.944	86.77	48.95
	D: 5.05	34	D: 5.05	106.70	1.95	0.964	94.61	50.53
	U: 6.33	47	U: 6.33	93.23	1.75	0.948	83.02	48.84
M1-N2	A: 1.02	12	A: 1.02	58.09	1.61	0.802	52.04	33.04
	B: 2.01	21	B: 2.01	63.59	1.75	0.892	56.63	33.40
	C: 3.98	39	C: 3.98	74.06	1.85	0.890	65.78	36.89
	D: 4.96	43	D: 4.96	68.07	1.79	0.938	60.55	34.99
	U: 6.21	48	U: 6.21	70.99	1.72	0.939	63.29	37.90
M1-N3	A: 1.05	8	A: 1.05	104.92	1.80	0.932	93.30	53.65
	B: 1.99	13	B: 1.99	128.20	2.63	0.887	113.90	46.61
	C: 3.96	21	C: 3.96	118.39	2.51	0.953	105.06	44.74
	D: 7.03	39	D: 7.03	128.67	2.07	0.967	113.98	57.84
	U: 8.47	41	U: 8.47	130.64	2.07	0.979	115.72	58.52
M2-N1	A: 1.09	6	A: 1.09	137.96	5.44	0.908	127.28	27.01
	B: 1.95	8	B: 1.95	169.55	6.94	0.873	158.53	26.87
	C: 5.04	21	C: 5.04	193.57	3.14	0.973	173.21	60.47
	D: 7.03	26	D: 7.03	196.24	3.01	0.959	175.26	63.57
	U: 9.17	28	U: 9.17	208.58	2.78	0.982	185.68	72.29
M3-N1	A: 1.05	4	A: 1.05	111.10	3.41	0.654	99.83	32.30
	B: 2.01	7	B: 2.01	149.33	2.46	0.909	132.45	57.43
	C: 4.93	18	C: 4.93	159.06	2.26	0.979	140.89	66.07
	D: 7.00	30	D: 7.00	141.30	1.81	0.971	125.62	71.79
	U: 8.56	34	U: 8.56	148.11	1.70	0.941	132.15	80.04

Figure 12 illustrates the variations in the mean crack width of ASUHPC for different Na_2CO_3 replacement quantities and activator modulus. With an increase in the Na_2CO_3 replacement quantity, the crack width of ASUHPC initially decreases and then increases at the same tensile strain. During the tensile process, the highest mean crack width of M1–N2 is only 65.78 μm, much lower than M1–N1 and M1–N3, which indicates that a certain amount of Na_2CO_3 helps reduce the crack width. However, when the Na_2CO_3 replacement quantity is further increased to 1.5 Na_2O%, the mean crack width in ASUHPC (M1-N3) increases to around 100 μm to 120 μm, which indicates that excessive Na_2CO_3 replacement quantity can reduce the crack control capability of ASUHPC. With an increase in activator modulus, the mean crack width of ASUHPC exceeds 100 μm. In particular, the mean crack width of M2–N1 reaches 185.68 μm in the ultimate stage, which leads us to observe that a high activator modulus is unfavorable for controlling crack width.

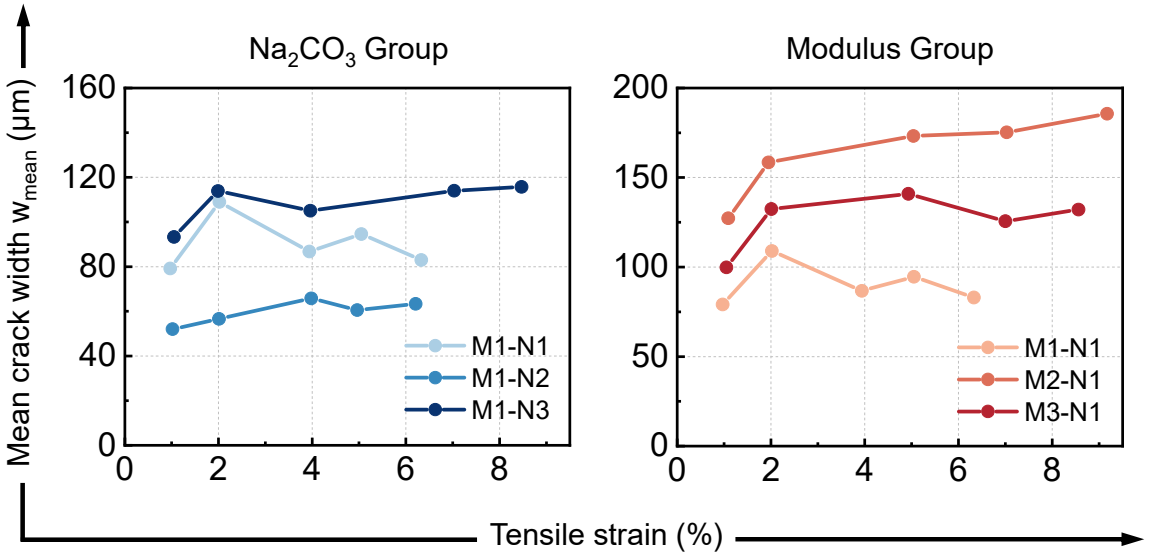

Figure 12. The relationship between mean crack width and tensile strain in ASUHPC for different Na_2CO_3 replacement quantities and activator modulus.

In showing the distribution characteristics of crack width in ASUHPC for different Na_2CO_3 replacement quantities and activator modulus, Figure 13 presents the probability density distribution and cumulative distribution curve of crack width in the ultimate tensile stage of ASUHPC. In the graph, it can be observed that a certain amount of Na_2CO_3 (0.75 Na_2O%) reduces both the crack width and width variability. Increasing the activator modulus widens the PDF curve and shifts the CDF curve to the right, significantly reducing the crack control capability of ASUHPC. This finding is consistent with the observations in Figure 11.

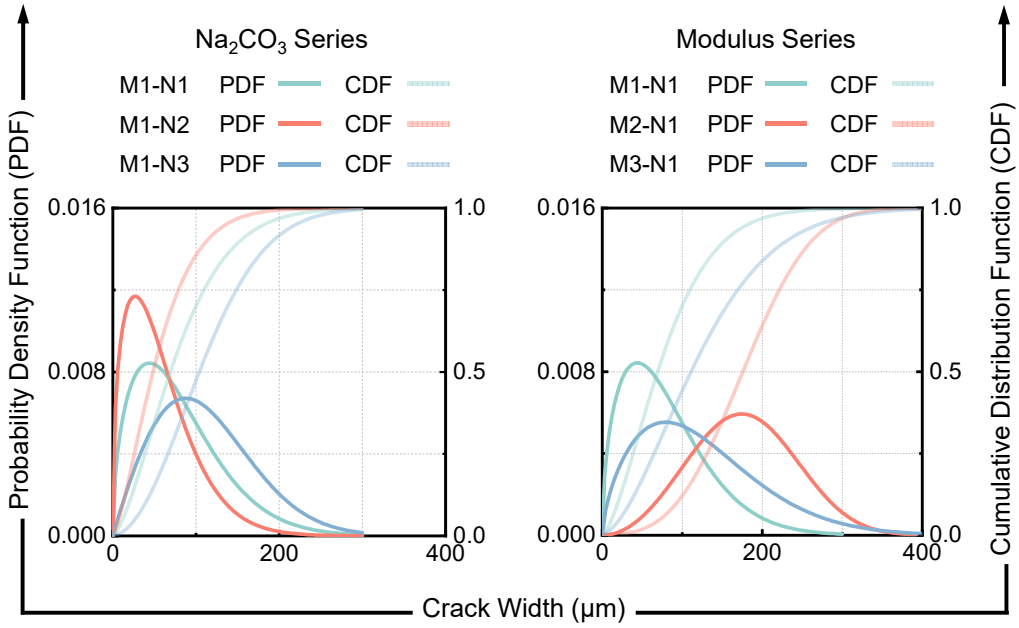

Figure 13. Weibull distribution (including probability density function (PDF) and cumulative distribution function (CDF)) of crack width in ASUHPC at the ultimate stage for different Na_2CO_3 replacement quantities and activator modulus.

3.3.2. Tensile Stress-Strain Curve

Figure 14 depicts the stress–strain curves of ASUHPC for different Na_2CO_3 replacement quantities and activator modulus. It can be observed in Figure 14 that variations in Na_2CO_3 replacement quantities and activator modulus significantly affect the stress fluctuations during the strain-hardening, initial cracking strength, tensile strength, and ultimate tensile strain stages of ASUHPC. In the strain-hardening stage, stress fluctuations are evident in ASUHPC. These fluctuations are mainly caused by the continuous initiation and stable propagation of cracks in ASUHPC, leading to stress redistribution as the tensile deformation increases. Among ASUHPC specimens with different Na_2CO_3 replacement quantities, M1–N2 exhibits the smallest amplitude of stress fluctuations during the strain-hardening stage, indicating better fiber bridging effects during crack initiation, which is consistent with the observation of the smallest average crack width in the M1–N2 sample. On the other hand, increasing the activator modulus has an opposite effect on stress fluctuations and crack control capability during the strain-hardening process of ASUHPC.

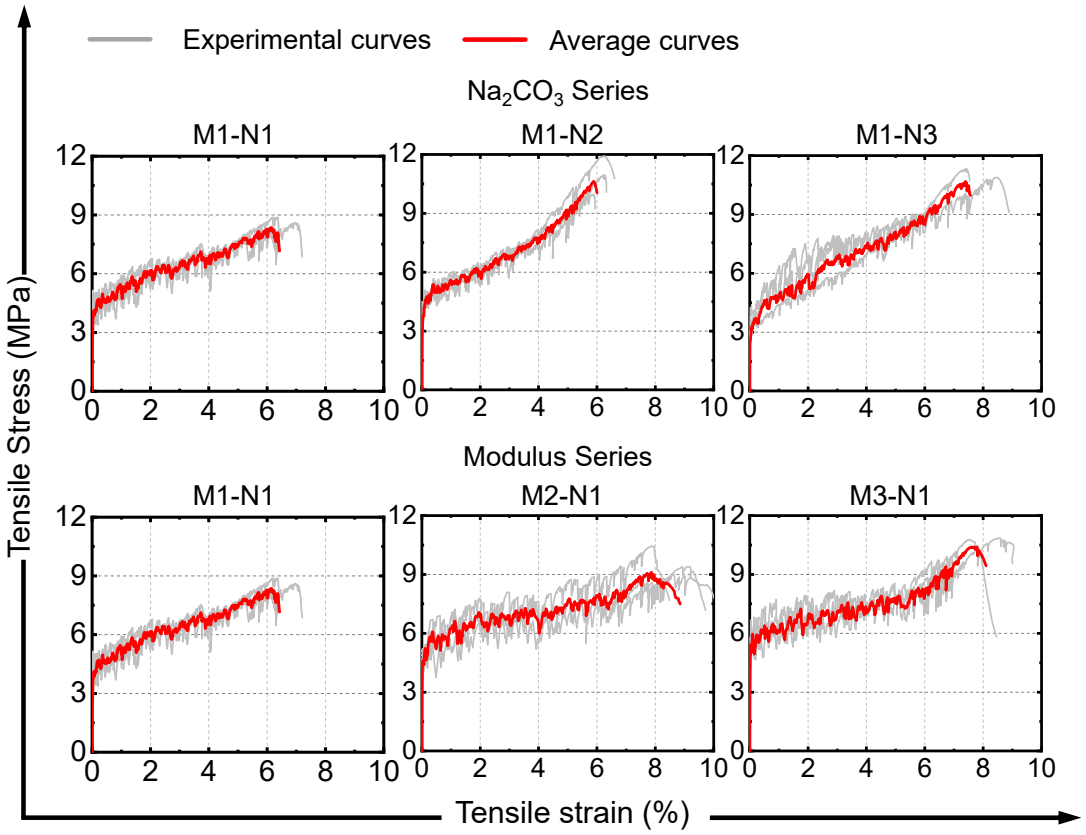

Figure 14. Tensile stress-strain curves of ASUHPC for different Na_2CO_3 replacement quantities and activator modulus.

Table 5 shows the Summary of tensile properties. Figure 15 illustrates the initial cracking strength, tensile strength, ultimate tensile strain, and tensile strain energy of ASUHPC for different Na_2CO_3 replacement quantities and activator modulus. In Figure 15a, it can be observed that the addition of Na_2CO_3 significantly reduces the initial cracking strength of ASUHPC. The initial cracking strength of M1–N3 is 3.17 MPa, which is a decrease of 31.7% compared to M1–N1. Conversely, in the modulus series, the initial cracking strength increases with the increase in modulus. Specifically, at a modulus of 1.65, the initial cracking strength of M3–N1 is 5.92 MPa, which is a 27.6% increase compared to M1–N1. According to the ECC design criteria [58], one of the prerequisites for

ECC to exhibit stable crack propagation is that the complementary energy (J_{tip}) exceeds the fracture energy of the matrix (J_b), with a higher pseudo strain-hardening coefficient (PSH) (i.e.,) indicating a more saturated crack distribution. A higher initial cracking strength implies a higher fracture toughness of the matrix [59–61]. Therefore, for M1–N2 with a Na_2CO_3 replacement quantity of 0.75 Na_2O%, the reduced initial cracking strength results in a more saturated crack distribution, compared to M1–N1. However, although the initial cracking strength of ASUHPC (M1–N3) continues to decrease with a further increase in the Na_2CO_3 replacement level, an excessive amount of Na_2CO_3 reduces the bridging effect between fibers and the matrix, thereby reducing the crack control capability of ASUHPC (manifested by fewer crack numbers and larger crack widths). For the modulus series, the significant increase in initial cracking strength noticeably diminishes the saturated crack behavior of ASUHPC, leading to a significant reduction in crack numbers.

In Figure 15b, it can be observed that the tensile strength of ASUHPC exceeds 8 MPa, and the use of Na_2CO_3 has a positive impact on the tensile strength. Both M1–N2 and M1–N3 exhibit tensile strengths exceeding 10 MPa, representing an improvement of 27.2% and 22.2%, respectively, compared to M1–N1.

Figure 15c shows that when the Na_2CO_3 replacement quantity is at 0.75 Na_2O%, the crack control capability of ASUHPC is improved, but the overall deformation capacity is limited, with M1–N2 reaching a limit strain of only 6.13%. Although increasing the activator modulus reduces crack control capability, M2–N1 exhibits the highest deformation capacity with a limit strain of 8.58%, representing a 31.6% increase, compared to M1-N1.

Figure 15d shows that in the Na_2CO_3 Series, M1–N2 exhibits a strain energy of only 416.8 kJ·m^{-3}, which is only 6.2% higher than M1–N1, as its ultimate strain is similar to M1–N1. However, when the Na_2CO_3 replacement reaches 1.5 Na_2O%, the strain energy of M1–N3 significantly increases to 518.5 kJ·m^{-3}, representing a 32.2% improvement, compared to M1–N1. Furthermore, in the modulus series, it can be observed that increasing the activator modulus significantly enhances the energy consumption capacity of ASUHPC. Both M2–N1 and M3–N1 exhibit higher strain energy due to increased deformation capacity. M3–N1 achieves a strain energy of 564.1 kJ·m^{-3}, which is 43.8% higher than M1–N1. In Figure 11, it can be observed that during the strain hardening stage, M3–N1 has larger crack widths and poorer crack control capability. However, it can fully utilize the bridging effect of fibers, achieving high energy consumption while reaching an ultimate strain of 7.66%.

The use of Na_2CO_3 reduces the initial cracking strength but benefits the tensile strength, while increasing the activator modulus enhances the initial cracking strength but reduces the crack control capability. On the basis of the above observations, we conclude that optimizing the cracking behavior and tensile properties of ASUHPC can be achieved by adjusting the replacement quantity of Na_2CO_3 and the modulus of the activator.

Table 5. Summary of tensile properties.

Mix IDs	Initial Cracking Stress, ε_c (MPa)	Tensile Strength, σ_u (MPa)	Ultimate Tensile Strain, ε_u (%)	Strain Energy, g_{se} (kJ·m^{-3})
M1-N1	4.64	8.60	6.52	392.3
M1-N2	3.92	10.94	6.13	416.8
M1-N3	3.17	10.51	7.38	518.5
M2-N1	4.74	9.64	8.58	553.6
M3-N1	5.92	10.50	7.66	564.1

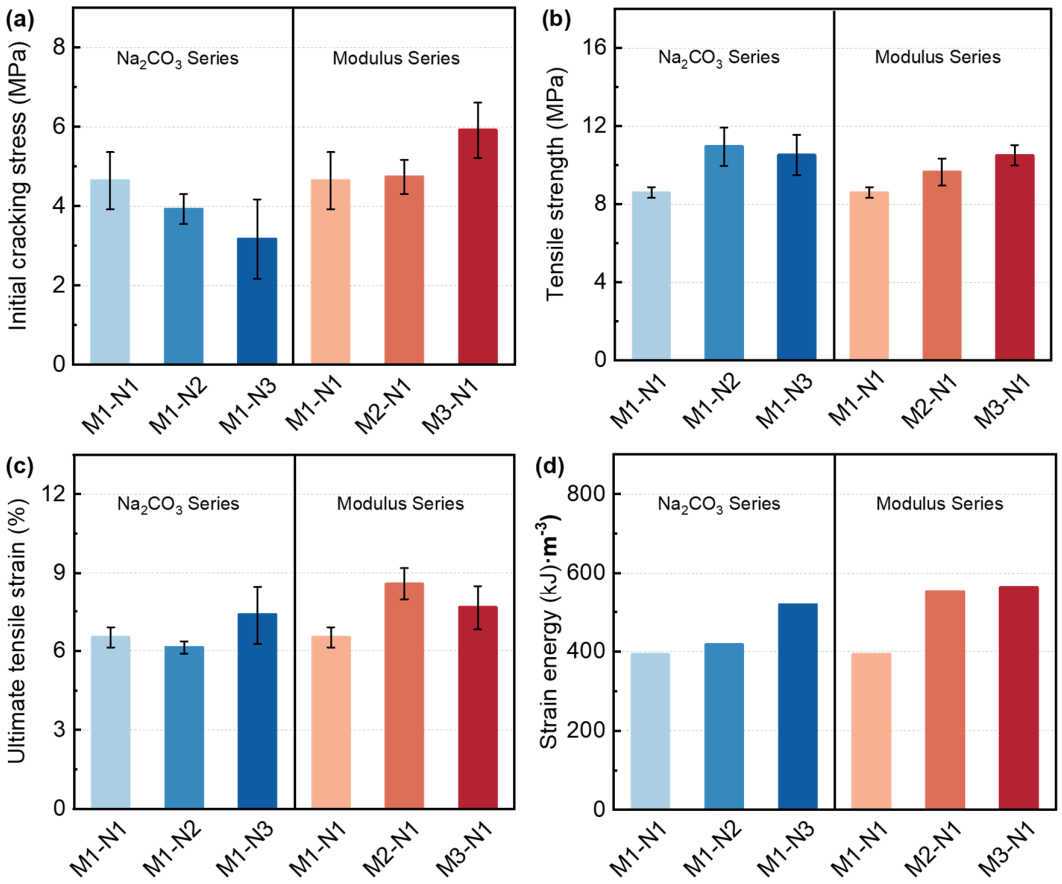

Figure 15. Tensile properties of ASUHPC for different Na_2CO_3 replacement quantities and activator modulus. (**a**) Initial cracking strength; (**b**) Tensile strength; (**c**) Ultimate tensile strain; (**d**) Tensile strain energy.

3.4. Mineral Characterization

3.4.1. X-ray Diffraction

Figure 15 shows the XRD patterns of the unreacted precursors and alkali-activated pastes for different Na_2CO_3 replacement quantities or activator modulus. In Figure 16a, significant broad scattering peaks can be observed for GGBS, FA, and SF, indicating their amorphous or partially crystalline nature. This is consistent with their amorphous properties, indicating good reactivity of the precursors. Crystalline peaks of Gehlenite (PDF# 96-900-4072) and Quartz (PDF# 01-079-2403) can be observed in the XRD pattern of GGBS and SF, respectively. FA exhibits higher crystallinity compared to GGBS and SF, showing multiple distinct crystalline peaks in the XRD pattern, including Mullite (PDF# 01-089-2644) and Quartz (PDF# 01-089-8937) phases [62].

Figure 16b and c display the XRD patterns of alkali-activated pastes for different Na_2CO_3 replacement quantities and activator modulus, all of which exhibit low-intensity crystalline peaks. In slag-fly ash-based geopolymers, the coexistence of aluminosilicates and hydrated calcium silicate is observed [63]. The main phase of aluminosilicate in the alkali-activated pastes is amorphous [64]. However, a distinct crystalline peak of hydrated calcium silicate (C-S-H, PDF# 00-033-0306) appears at approximately 29° 2θ. Figure 16b shows that the crystalline peak of C-S-H intensifies with an increase in Na_2CO_3 replacement quantity. This may also be one of the reasons for the improvement in compressive strength as the replacement quantity of Na_2CO_3 increases. Additionally, Vaterite ($CaCO_3$, PDF# 01-072-0506) crystalline phase is observed in M1–N2, but disappears in alkali-activated pastes with higher Na_2CO_3 replacement quantity, and Calcite ($CaCO_3$, PDF# 01-086-

23346) appears instead. This is because it is easier to form Vaterite with larger particle size in undersaturated carbonate solutions, while Calcite is more likely to form in saturated carbonate solutions [65]. The relatively low-density Vaterite and Calcite phases may cause localized expansion in the matrix, reducing the matrix's fracture toughness, and consequently lowering the initial cracking strength of ASUHPC. In Figure 16c, it can be observed that the crystalline phases of the alkali-activated pastes remain relatively unchanged within the range of activator modulus from 1.35 to 1.65.

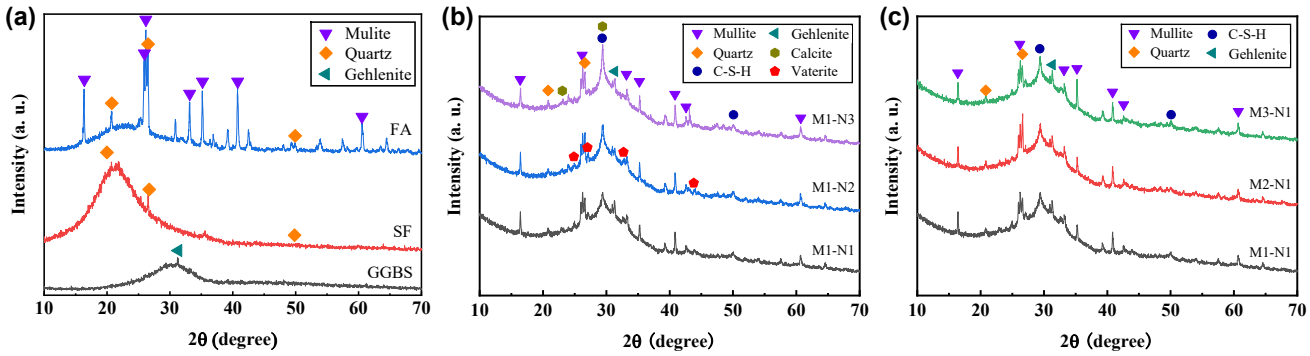

Figure 16. The XRD patterns of the unreacted precursors and alkali-activated pastes for different Na_2CO_3 replacement quantities or activator modulus. (**a**) XRD patterns of unreacted precursors (GGBS, FA, and SF); (**b**) XRD patterns of alkali-activated pastes for different Na_2CO_3 replacement quantities; (**c**) XRD patterns of alkali-activated pastes for different activator modulus.

3.4.2. Scanning Electron Microscopy

The SEM images in Figure 17 depict the fiber failure modes on the fracture surface of ASUHPC. The fiber failure modes in the ASUHPC fracture surface are primarily fiber pull-out and fiber fracture (see Figure 17a). In Figure 17b, it can be observed that different Na_2CO_3 replacement quantities and activator modulus have a significant influence on the fiber failure modes of the ASUHPC fracture surface. In M1–N1, most fibers experience pull-out failure, with only a few fibers exhibiting fracture. After partially replacing NaOH-Na_2SiO_3 activator with Na_2CO_3, the proportion of fibers experiencing pull-out and fracture failure is significantly reduced in M1–N2 and M1–N3 specimens. The use of Na_2CO_3 enhances the fiber-matrix bond strength in ASUHPC, leading to higher tensile strength in M1–N2 and M1–N3, compared to M1–N1. This may be attributed to the improved density of the paste, as indicated in Figure 11. Additionally, Figure 17b demonstrates that increasing the activator modulus also reduces the proportion of fibers experiencing pull-out and fracture failure in the specimens. As a result, M2–N1 and M3–N1 exhibit slightly higher tensile strength, compared to M1–N1.

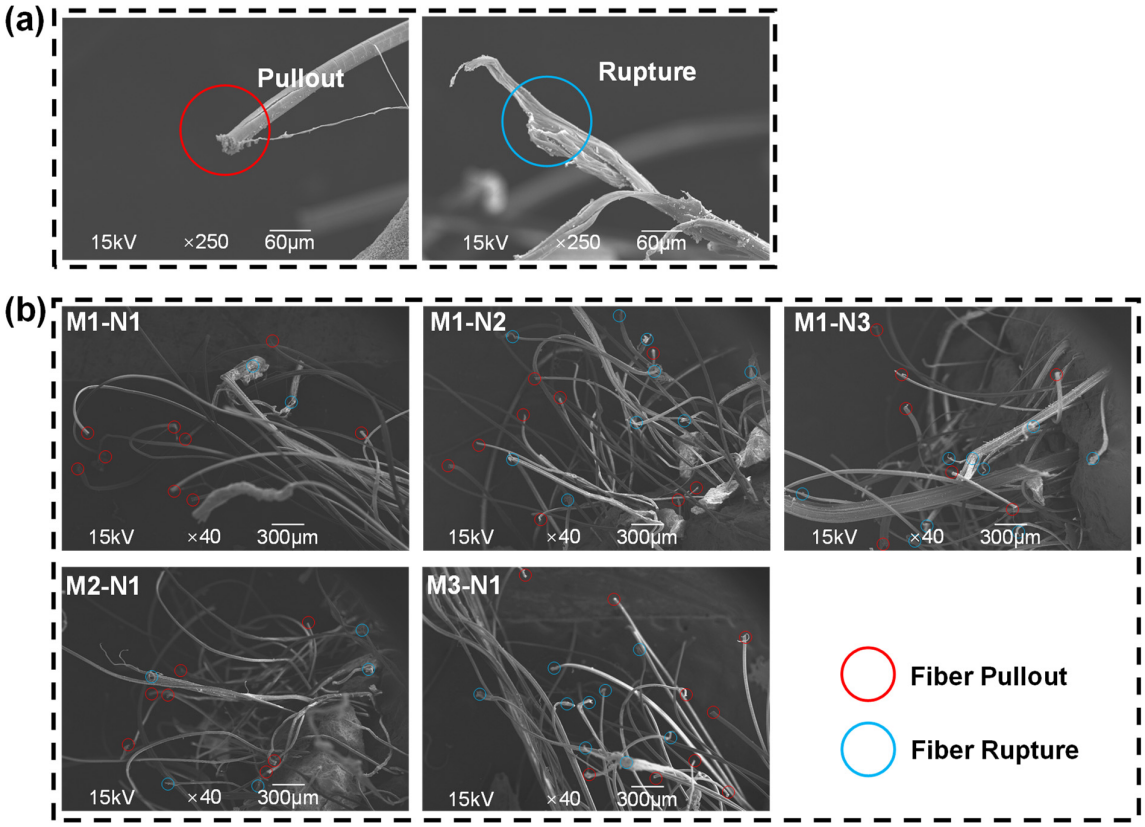

Figure 17. Fiber failure modes of the fracture surface of ASUHPC. (**a**) Typical fiber failure modes, including fiber pull-out failure and fiber fracture failure; (**b**) Fiber failure modes of the fracture surface of ASUHPC for different Na_2CO_3 replacement quantities and activator modulus.

Figure 18 presents the SEM images of different alkali-activated pastes. It can be observed that all alkali-activated pastes contain unhydrated fly ash and slag embedded in the alkali-activated gel. In Figure 18a, it can be seen that the M1–N1 paste is relatively dense with fewer microcracks, and the width and length of cracks are small. However, with the partial replacement of NaOH-Na_2SiO_3 activator by Na_2CO_3, the width of cracks in the paste increases, and M1–N3 exhibits distinct cracks with a width of approximately 5 μm. Similarly, increasing the activator modulus also leads to an increase in crack width and significant elongation of cracks, which is consistent with previous research findings [66]. Figure 18b shows the morphology of Na_2CO_3 series pastes in two different magnifications. At a magnification of 2000, the presence of calcium carbonate crystals near the microcracks is observed in M1–N2 and M1–N3 pastes. The irregularly shaped low-crystallinity calcium carbonate, due to its low density, large deposition volume, and small size, causes differential expansion in certain aggregation regions, leading to the occurrence of microcracks in alkali-activated pastes [42]. The expansion of calcite in the aggregation regions may be one of the reasons for the reduction in the initial crack strength of M1–N2 and M1–N3 under tensile.

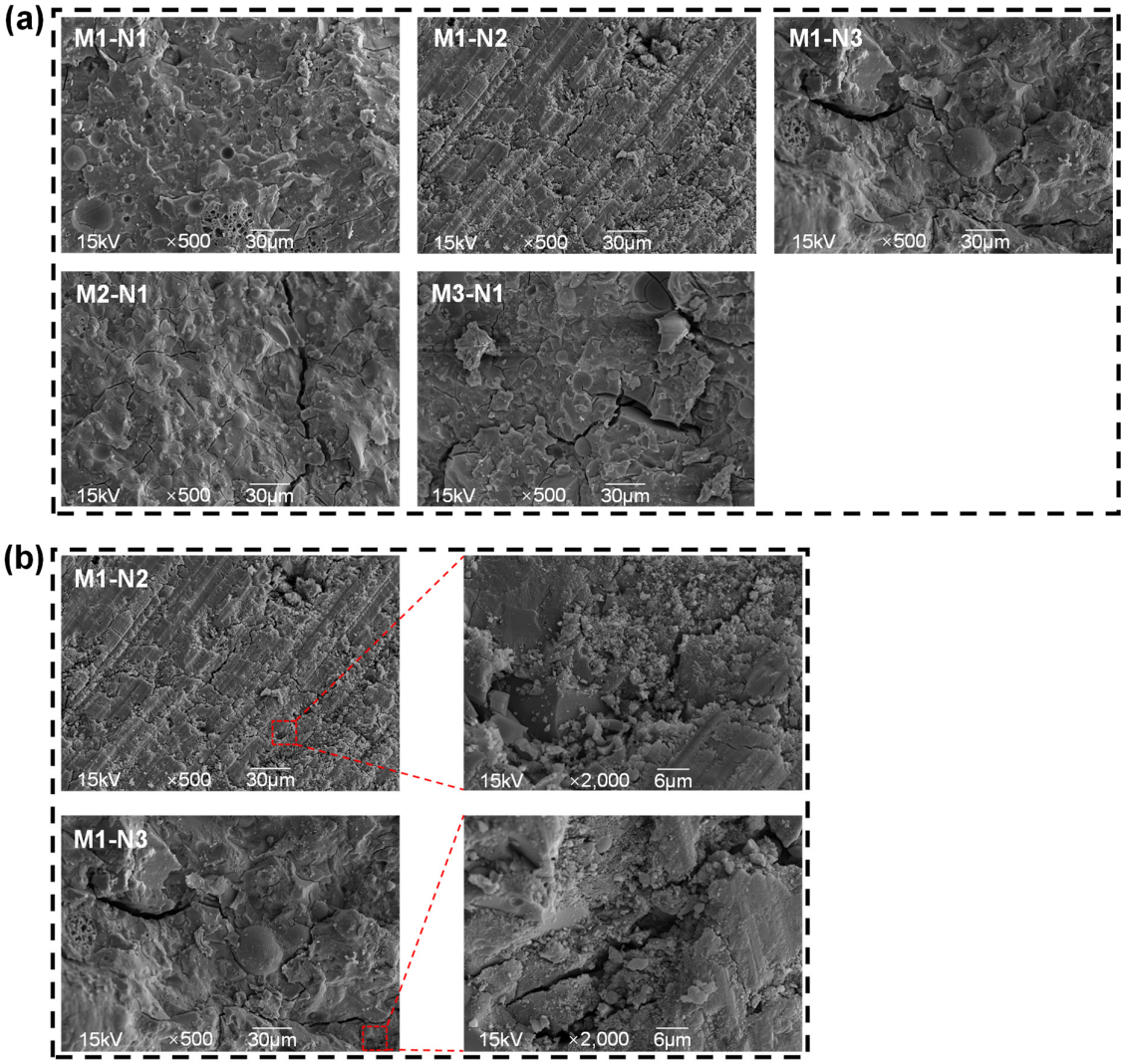

Figure 18. SEM images of alkali-activated pastes. (**a**) Microstructure morphology of alkali-activated pastes for different Na_2CO_3 replacement quantities and activator modulus; (**b**) Distribution of $CaCO_3$ in alkali-activated pastes with different Na_2CO_3 replacement quantities.

4. Environmental Benefit Analysis

The use of Na_2CO_3 significantly reduces the consumption of NaOH–Na_2SiO_3 solution and NaOH, which is of great significance for reducing the carbon emissions of alkali-activated concrete. In order to quantify the impact of activator variations on the environmental performance of ASUHPC, this section comprehensively discusses the environmental performance of ASUHPC by considering both its tensile properties and carbon emissions, using the ratio of tensile properties to CO_2-e to represent environmental benefit indices, and thus evaluate its environmental benefits. Table 6 presents the carbon emission factors and total carbon emissions per cubic meter of ASUHPC used in this study. It should be noted that the carbon emission factors of raw materials only consider the carbon emissions generated during their production process.

Table 6. Carbon emission factor of raw materials and CO_2-e per m^3 concrete. (kg CO_2-e/kg).

Materials	Emission Factor (kg CO_2-e/kg)	Mix IDs					Reference
		M1–N1	M1–N2	M1–N3	M2–N1	M3–N1	
GGBS	0.019	15.58	15.58	15.58	15.58	15.58	[67]
FA	0.009	2.237	2.237	2.237	2.237	2.237	[67]
SF	0	0	0	0	0	0	[68]
NaOH	1.915	83.96	75.27	66.32	69.83	55.61	[68]
Na_2SiO_3	1.222	433.3	388.1	342.5	479.2	524.8	[68]
Na_2CO_3	0.111	/	1.657	3.325	/	/	[69]
QS	0.01	4.066	4.066	4.066	4.066	4.066	[67]
PE fiber	2	38.80	38.80	38.80	38.80	38.80	[70]
CO_2-e (kg CO_2-e/m^3)	/	578.0	525.7	472.9	609.7	641.1	/

Figure 19 illustrates the carbon emissions of each raw material and the total carbon emissions per cubic meter of ASUHPC. The graph shows that the activator contributes the most to the carbon emissions of ASUHPC raw materials, accounting for over 87%. In M1–N1, Na_2SiO_3 accounts for 75.0% of the total carbon emissions, while the carbon emissions from the NaOH–Na_2SiO_3 activator reach 89.5%. The carbon emissions of M1–N1 amount to 578.0 kg CO_2-e/m3, but the use of Na_2CO_3 to partially replace the activator significantly reduces the carbon emissions of ASUHPC, with M1–N3 reducing by 18.2%, compared to M1–N1. On the other hand, increasing the activator modulus means increasing the dosage of Na_2SiO_3, which leads to higher carbon emissions. When the activator modulus is increased to 1.65, the carbon emissions of M2–N1 reach 641.1 kg CO_2-e/m3, representing a 10.9% increase.

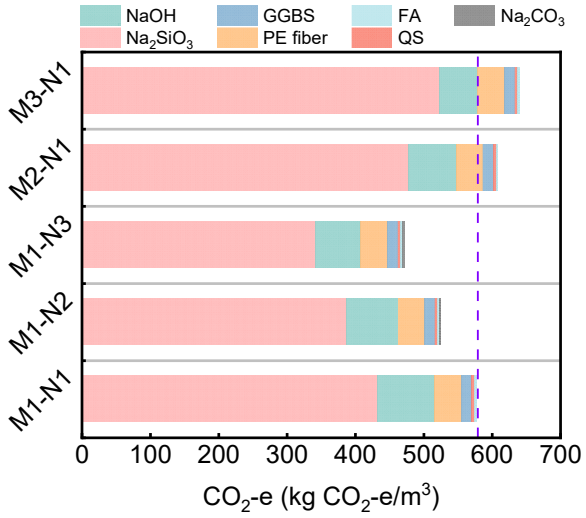

Figure 19. The total carbon emissions and composition per cubic meter of ASUHPC.

The carbon emissions of ASUHPC are normalized, assuming the CO_2-e value of M1–N1 as one unit. The CO_2-e values for M1–N2, M1–N3, M2–N1, and M3–N1 are 0.91, 0.82, 1.05, and 1.11, respectively. The ratio of tensile strength, ultimate tensile strain, and strain energy to CO_2-e is used as an environmental benefit index and plotted on a three-dimensional radar chart to evaluate the environmental performance of ASUHPC (see Figure 20). In Figure 20, it can be observed that M2–N1 and M3–N1 have the largest enclosed area, indicating the most outstanding overall environmental performance. Although M1–N2

has the lowest CO_2-e value, its inferior tensile performance diminishes its overall environmental performance, with only the σ_u/CO_2-e index standing out, compared to M1–N1.

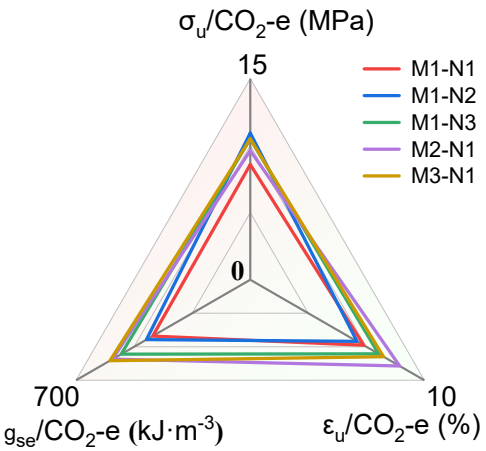

Figure 20. Radar chart of environmental indices: σ_u/CO_2-e; ε_u/CO_2-e; g_{se}/CO_2-e.

However, the evaluation of overall environmental performance alone cannot fully determine the superiority or inferiority of different ASUHPC mixes. M1–N2 demonstrates good crack control capability during the strain hardening stage, with crack widths consistently below 100 μm throughout the entire tensile process, which is beneficial for improving the durability of concrete structures [71]. Although M2–N1 and M3–N1 exhibit superior mechanical properties, their crack control capability is relatively lower, making them suitable for structures that do not require high durability.

5. Conclusions

This study further advanced the development of high-performance alkali-activated concrete by proposing alkali-activated-strain-hardening-ultra-high-performance concrete (ASUHPC) and attempting to achieve its low carbonization through the use of sodium carbonate as a supplementary activator. The study investigated the influence of Na_2CO_3 replacement quantity and activator modulus on the fresh and hardened properties of ASUHPC, and also evaluated its environmental performance. The following conclusions can be drawn:

(1) The setting time of the fresh alkali-activated paste is prolonged with increasing Na_2CO_3 replacement quantity and activator modulus. The use of Na_2CO_3 delays the formation of the polymerization product, thereby delaying the setting of the paste. Different particle size distributions are observed in the fresh alkali-activated pastes due to varying levels of Na_2CO_3 replacement quantity and activator modulus. Increasing the Na_2CO_3 replacement quantity optimizes the particle size distribution and improves the density of the matrix, while increasing the sodium silicate modulus has a negative effect on the density.

(2) The compressive strength of all ASUHPC mixtures exceeds 120 MPa, and the variation in compressive strength follows the same trend as the density variation in fresh alkali-activated pastes. The highest compressive strength of 126.7 MPa is achieved when the Na_2CO_3 replacement quantity is 1.5 Na_2O%, which corresponds to the highest density in the fresh paste.

(3) The crack width during the tensile process of ASUHPC follows a Weibull distribution. The use of Na_2CO_3 improves the saturated crack behavior of ASUHPC. When the Na_2CO_3 replacement quantity is 0.75 Na_2O%, the crack control capability is the best, with the highest number of cracks and the maximum average crack width during the tensile process only reaching 65.78 μm. On the other hand, increasing the modulus of the activator significantly weakens the crack control capability of ASUHPC, leading to an increase in crack width.

(4) The use of Na_2CO_3 as a supplementary activator can effectively reduce the initial cracking strength of ASUHPC. This may increase the pseudo-strain hardening coefficient of ASUHPC, resulting in better saturated crack behavior. Increasing the modulus of sodium silicate improves the initial cracking strength, which reduces the crack control capability of ASUHPC but also increases the area enclosed by the stress-strain curve. Therefore, when the activator modulus is 1.65, the strain energy of ASUHPC reaches 564.1 kJ·m-3, which is a 43.8% increase, compared to when the modulus is 1.35.

(5) XRD analysis revealed that the crystalline peaks of the C-S-H phase were enhanced with increasing Na_2CO_3 replacement quantity. Different crystalline phases of $CaCO_3$ were observed in different Na_2CO_3 replacement quantities, with Vaterite and Calcite present in M1–N2 and M1–N3, respectively. SEM analysis revealed that increasing the Na_2CO_3 replacement quantity and activator modulus resulted in a higher proportion of fiber fracture in the fracture surface of ASUHPC, which indicates an enhancement of fiber bridging effect.

(6) Although the use of Na_2CO_3 effectively reduces carbon emissions, with a reduction of 18.2% observed when the Na_2CO_3 replacement quantity is at 1.5 Na_2O%, a comprehensive analysis considering key tensile properties, such as tensile strength, ultimate tensile strain, and tensile strain energy, reveals that increasing the activator modulus yields better environmental performance. However, in applications that require higher durability, ASUHPC with a Na_2CO_3 replacement quantity of 0.75 Na_2O% is evidently more suitable.

Author Contributions: Conceptualization, K.-X.Z.; methodology, K.-X.Z.; formal analysis, J.-X.L.; investigation, K.-X.Z. and J.-X.L.; resources, J.-X.L.; data curation, G.C. and R.-H.L.; writing—original draft preparation, K.-X.Z.; writing—review and editing, K.-X.Z. and G.C.; visualization, R.-H.L., Y.-W.C. and D.-H.L.; funding acquisition, J.-X.L. All authors have read and agreed to the published version of the manuscript.

Funding: This research was funded by the National Natural Science Foundation of China (grant number 12002090).

Data Availability Statement: The data presented in this study are available on request from the corresponding author. The data are not publicly available due to confidentiality issues.

Conflicts of Interest: Author Yi-Wu Chen was employed by the company Guangdong Jialin Construction Co., Ltd. Author De-Hui Li was employed by the company Guangdong Shenghong Construction Engineering Co., Ltd. The remaining authors declare that the research was conducted in the absence of any commercial or financial relationships that could be construed as a potential conflict of interest.

References

1. Van Damme, H. Concrete material science: Past, present, and future innovations. *Cem. Concr. Res.* **2018**, *112*, 5–24. https://doi.org/10.1016/j.cemconres.2018.05.002.
2. Xi, B.; Al-Obaidi, S.; Ferrara, L. Effect of different environments on the self-healing performance of Ultra High-Performance Concrete—A systematic literature review. *Constr. Build. Mater.* **2023**, *374*, 130946. https://doi.org/10.1016/j.conbuildmat.2023.130946.
3. Wang, S.; Wang, B.; Zhu, H.; Chen, G.; Li, Z.; Yang, L.; Zhang, Y.; Zhou, X. Ultra-high performance concrete: Mix design, raw materials and curing regimes-A review. *Mater. Today Commun.* **2023**, *35*, 105468. https://doi.org/10.1016/j.mtcomm.2023.105468.
4. Li, L.; Wang, B.; Hubler, M.H. Carbon nanofibers (CNFs) dispersed in ultra-high performance concrete (UHPC): Mechanical property, workability and permeability investigation. *Cem. Concr. Compos.* **2022**, *131*, 104592. https://doi.org/10.1016/j.cemconcomp.2022.104592.
5. Yu, R.; Spiesz, P.; Brouwers, H. Development of an eco-friendly Ultra-High Performance Concrete (UHPC) with efficient cement and mineral admixtures uses. *Cem. Concr. Compos.* **2015**, *55*, 383–394. https://doi.org/10.1016/j.cemconcomp.2014.09.024.
6. Lin, J.-X.; Su, J.-Y.; Pan, H.-S.; Peng, Y.-Q.; Guo, Y.-C.; Chen, W.-S.; Sun, X.-L.; Yuan, B.-X.; Liu, G.-T.; Lan, X.-W. Dynamic compression behavior of ultra-high performance concrete with hybrid polyoxymethylene fiber and steel fiber. *J. Mater. Res. Technol.* **2022**, *20*, 4473–4486. https://doi.org/10.1016/j.jmrt.2022.08.139.
7. Akeed, M.H.; Qaidi, S.; Ahmed, H.U.; Faraj, R.H.; Mohammed, A.S.; Emad, W.; Tayeh, B.A.; Azevedo, A.R. Ultra-high-performance fiber-reinforced concrete. Part IV: Durability properties, cost assessment, applications, and challenges. *Case Stud. Constr. Mater.* **2022**, *17*, e01271. https://doi.org/10.1016/j.cscm.2022.e01271.

8. Ganesh, P.; Murthy, A.R. Tensile behaviour and durability aspects of sustainable ultra-high performance concrete incorporated with GGBS as cementitious material. *Constr. Build. Mater.* **2018**, *197*, 667–680. https://doi.org/10.1016/j.conbuildmat.2018.11.240.
9. Lin, J.-X.; Song, Y.; Xie, Z.-H.; Guo, Y.-C.; Yuan, B.; Zeng, J.-J.; Wei, X. Static and dynamic mechanical behavior of engineered cementitious composites with PP and PVA fibers. *J. Build. Eng.* **2019**, *29*, 101097. https://doi.org/10.1016/j.jobe.2019.101097.
10. Zhu, H.; Hu, W.-H.; Mehthel, M.; Villette, T.; Vidal, O.S.; Nasser, W.N.; Li, V.C. Engineered cementitious composites (ECC) with a high volume of volcanic ash: Rheological, mechanical, and micro performance. *Cem. Concr. Compos.* **2023**, *139*, 105051. https://doi.org/10.1016/j.cemconcomp.2023.105051.
11. Lương, Q.-H.; Nguyễn, H.H.; Nguyễn, P.H.; Kang, S.-T.; Lee, B.Y. Extremely-ductile alkali-activated slag-based composite with a tensile strain capacity up to 22%. *Ceram. Int.* **2023**, *49*, 12069–12078. https://doi.org/10.1016/j.ceramint.2022.12.057.
12. Liu, H.; Zhang, Q.; Li, V.; Su, H.; Gu, C. Durability study on engineered cementitious composites (ECC) under sulfate and chloride environment. *Constr. Build. Mater.* **2017**, *133*, 171–181. https://doi.org/10.1016/j.conbuildmat.2016.12.074.
13. Suryanto, B.; Tambusay, A.; Suprobo, P.; Bregoli, G.; Aitken, M. Seismic performance of exterior beam-column joints constructed with engineered cementitious composite: Comparison with ordinary and steel fibre reinforced concrete. *Eng. Struct.* **2022**, *250*, 113377. https://doi.org/10.1016/j.engstruct.2021.113377.
14. Kunieda, M.; Hussein, M.; Ueda, N.; Nakamura, H. Enhancement of Crack Distribution of UHP-SHCC under Axial Tension Using Steel Reinforcement. *J. Adv. Concr. Technol.* **2010**, *8*, 49–57. https://doi.org/10.3151/jact.8.49.
15. Park, S.H.; Kim, D.J.; Ryu, G.S.; Koh, K.T. Tensile behavior of Ultra High Performance Hybrid Fiber Reinforced Concrete. *Cem. Concr. Compos.* **2012**, *34*, 172–184. https://doi.org/10.1016/j.cemconcomp.2011.09.009.
16. Wille, K.; Kim, D.J.; Naaman, A.E. Strain-hardening UHP-FRC with low fiber contents. *Mater. Struct.* **2011**, *44*, 583–598. https://doi.org/10.1617/s11527-010-9650-4.
17. Ranade, R.; Li, V.; Stults, M.D.; Heard, T.W.; Rushing, T. Composite Properties of High-Strength, High-Ductility Concrete. *ACI Mater. J.* **2013**, *110*, 413–422. https://doi.org/10.14359/51685788.
18. Yu, K.-Q.; Yu, J.-T.; Dai, J.-G.; Lu, Z.-D.; Shah, S.P. Development of ultra-high performance engineered cementitious composites using polyethylene (PE) fibers. *Constr. Build. Mater.* **2018**, *158*, 217–227. https://doi.org/10.1016/j.conbuildmat.2017.10.040.
19. Huntzinger, D.N.; Eatmon, T.D. A life-cycle assessment of Portland cement manufacturing: Comparing the traditional process with alternative technologies. *J. Clean. Prod.* **2009**, *17*, 668–675. https://doi.org/10.1016/j.jclepro.2008.04.007.
20. Chen, G.; Zheng, D.-P.; Chen, Y.-W.; Lin, J.-X.; Lao, W.-J.; Guo, Y.-C.; Chen, Z.-B.; Lan, X.-W. Development of high performance geopolymer concrete with waste rubber and recycle steel fiber: A study on compressive behavior, carbon emissions and economical performance. *Constr. Build. Mater.* **2023**, *393*, 131988. https://doi.org/10.1016/j.conbuildmat.2023.131988.
21. Fu, Q.; Xu, W.; Zhao, X.; Bu, M.; Yuan, Q.; Niu, D. The microstructure and durability of fly ash-based geopolymer concrete: A review. *Ceram. Int.* **2021**, *47*, 29550–29566. https://doi.org/10.1016/j.ceramint.2021.07.190.
22. Shobeiri, V.; Bennett, B.; Xie, T.; Visintin, P. A comprehensive assessment of the global warming potential of geopolymer concrete. *J. Clean. Prod.* **2021**, *297*, 126669. https://doi.org/10.1016/j.jclepro.2021.126669.
23. Nematollahi, B.; Qiu, J.; Yang, E.-H.; Sanjayan, J. Micromechanics constitutive modelling and optimization of strain hardening geopolymer composite. *Ceram. Int.* **2017**, *43*, 5999–6007. https://doi.org/10.1016/j.ceramint.2017.01.138.
24. Ambily, P.S.; Ravisankar, K.; Umarani, C.; Dattatreya, J.K.; Iyer, N.R. Development of ultra-high-performance geopolymer concrete. *Mag. Concr. Res.* **2014**, *66*, 82–89. https://doi.org/10.1680/macr.13.00057.
25. Wang, F.; Sun, X.; Tao, Z.; Pan, Z. Effect of silica fume on compressive strength of ultra-high-performance concrete made of calci-um aluminate cement/fly ash based geopolymer. *J. Build. Eng.* **2022**, *62*, 105398. https://doi.org/10.1016/j.jobe.2022.105398.
26. Liu, Y.; Zhang, Z.; Shi, C.; Zhu, D.; Li, N.; Deng, Y. Development of ultra-high performance geopolymer concrete (UHPGC): Influence of steel fiber on mechanical properties. *Cem. Concr. Compos.* **2020**, *112*, 103670. https://doi.org/10.1016/j.cemconcomp.2020.103670.
27. Kan, L.-L.; Wang, W.-S.; Liu, W.-D.; Wu, M. Development and characterization of fly ash based PVA fiber reinforced Engineered Geopolymer Composites incorporating metakaolin. *Cem. Concr. Compos.* **2020**, *108*, 103521. https://doi.org/10.1016/j.cemconcomp.2020.103521.
28. Alfimova, N.; Kozhukhova, N.; Zhernovskaya, I.; Shurakov, I.; Kozhukhova, M. *Using of Citrogypsum in Alkali Activated Systems*; Springer: Cham, Switzerland, 2023; Volume 307, pp. 17–22. https://doi.org/10.1007/978-3-031-20459-3_3.
29. Sanyin, Z.; Qijun, Y.; Fei, Q.; Jiaqi, H.; Suhong, Y.; Ziyun, W.; Guobang, G. Setting and strength characteristics of alkali-activated carbonatite cementitious materials with ground slag replacement. *J. Wuhan Univ. Technol. Sci. Ed.* **2006**, *21*, 125–128. https://doi.org/10.1007/bf02861489.
30. Lao, J.-C.; Xu, L.-Y.; Huang, B.-T.; Dai, J.-G.; Shah, S.P. Strain-hardening Ultra-High-Performance Geopolymer Concrete (UHPGC): Matrix design and effect of steel fibers. *Compos. Commun.* **2022**, *30*, 101081. https://doi.org/10.1016/j.coco.2022.101081.
31. Ohno, M.; Li, V.C. A feasibility study of strain hardening fiber reinforced fly ash-based geopolymer composites. *Constr. Build. Mater.* **2014**, *57*, 163–168. https://doi.org/10.1016/j.conbuildmat.2014.02.005.
32. Kozhukhova, N.I.; Alfimova, N.I.; Kozhukhova, M.I.; Nikulin, I.S.; Glazkov, R.A.; Kolomytceva, A.I. The Effect of Recycled Citrogypsum as a Supplementary Mineral Additive on the Physical and Mechanical Performance of Granulated Blast Furnace Slag-Based Alkali-Activated Binders. *Recycling* **2023**, *8*, 22. https://doi.org/10.3390/recycling8010022.
33. Li, N.; Shi, C.; Zhang, Z.; Zhu, D.; Hwang, H.-J.; Zhu, Y.; Sun, T. A mixture proportioning method for the development of performance-based alkali-activated slag-based concrete. *Cem. Concr. Compos.* **2018**, *93*, 163–174. https://doi.org/10.1016/j.cemconcomp.2018.07.009.

34. Mousavinejad, S.H.G.; Sammak, M. An assessment of the effect of Na_2SiO_3/NaOH ratio, NaOH solution concentration, and aging on the fracture properties of ultra-high-performance geopolymer concrete: The application of the work of fracture and size effect methods. *Structures* **2022**, *39*, 434–443. https://doi.org/10.1016/j.istruc.2022.03.045.
35. Alsalman, A.; Assi, L.N.; Kareem, R.S.; Carter, K.; Ziehl, P. Energy and CO_2 emission assessments of alkali-activated concrete and Ordinary Portland Cement concrete: A comparative analysis of different grades of concrete. *Clean. Environ. Syst.* **2021**, *3*, 100047. https://doi.org/10.1016/j.cesys.2021.100047.
36. Rathod, N.; Chippagiri, R.; Ralegaonkar, R.V. Cleaner production of geopolymer materials: A critical review of waste-derived activators. *Mater. Today Proc.* **2023**, *in press*. https://doi.org/10.1016/j.matpr.2023.03.502.
37. Sandanayake, M.; Gunasekara, C.; Law, D.; Zhang, G.; Setunge, S. Greenhouse gas emissions of different fly ash based geopolymer concretes in building construction. *J. Clean. Prod.* **2018**, *204*, 399–408. https://doi.org/10.1016/j.jclepro.2018.08.311.
38. Luo, Q.; Liu, Y.; Dong, B.; Ren, J.; He, Y.; Wu, K.; Wang, Y. Lithium slag-based geopolymer synthesized with hybrid solid activators. *Constr. Build. Mater.* **2023**, *365*, 130070. https://doi.org/10.1016/j.conbuildmat.2022.130070.
39. Neupane, K. Evaluation of environmental sustainability of one-part geopolymer binder concrete. *Clean. Mater.* **2022**, *6*, 100138. https://doi.org/10.1016/j.clema.2022.100138.
40. Al-Noaimat, Y.A.; Ghaffar, S.H.; Chougan, M.; Al-Kheetan, M.J. A review of 3D printing low-carbon concrete with one-part geopolymer: Engineering, environmental and economic feasibility. *Case Stud. Constr. Mater.* **2023**, *18*, e01818. https://doi.org/10.1016/j.cscm.2022.e01818.
41. Zheng, Y.; Rao, F.; Yang, L.; Zhong, S. Comparison of ternary and dual combined waste-derived alkali activators on the durability of volcanic ash-based geopolymers. *Cem. Concr. Compos.* **2023**, *136*, 104886. https://doi.org/10.1016/j.cemconcomp.2022.104886.
42. Ma, C.; Zhao, B.; Guo, S.; Long, G.; Xie, Y. Properties and characterization of green one-part geopolymer activated by composite activators. *J. Clean. Prod.* **2019**, *220*, 188–199. https://doi.org/10.1016/j.jclepro.2019.02.159.
43. Wang, Y.-S.; Alrefaei, Y.; Dai, J.-G. Roles of hybrid activators in improving the early-age properties of one-part geopolymer pastes. *Constr. Build. Mater.* **2021**, *306*, 124880. https://doi.org/10.1016/j.conbuildmat.2021.124880.
44. Bian, Z.; Jin, G.; Ji, T. Effect of combined activator of $Ca(OH)_2$ and Na_2CO_3 on workability and compressive strength of alkali-activated ferronickel slag system. *Cem. Concr. Compos.* **2021**, *123*, 104179. https://doi.org/10.1016/j.cemconcomp.2021.104179.
45. Burciaga-Díaz, O.; Betancourt-Castillo, I.; Montes-Escobedo, M.; Escalante-García, J. One-part pastes and mortars of CaO-Na_2CO_3 activated blast furnace slag: Microstructural evolution, cost and CO_2 emissions. *Constr. Build. Mater.* **2023**, *368*, 130431. https://doi.org/10.1016/j.conbuildmat.2023.130431.
46. *GB/T 18046-2017*; Ground Granulated Blast Furnace Slag Used for Cement and Concrete. China Architecture & Building Press: Beijing, China, 2017.
47. *ASTM C618-2019*; Standard Specification for Coal Fly Ash and Raw or Calcined Natural Pozzolan for Use in Concrete. ASTM International: West Conshohocken, PA, USA, 2019.
48. Ye, N.; Yang, J.; Liang, S.; Hu, Y.; Hu, J.; Xiao, B.; Huang, Q. Synthesis and strength optimization of one-part geopolymer based on red mud. *Constr. Build. Mater.* **2016**, *111*, 317–325. https://doi.org/10.1016/j.conbuildmat.2016.02.099.
49. Shen, W.; Zhou, M.; Xiao, L.; Ma, W.; Cai, Z. Morphology difference between the alkali activated cement and portland cement paste on multi-scale. *J. Wuhan Univ. Technol. Sci. Ed.* **2008**, *23*, 923–926. https://doi.org/10.1007/s11595-007-6923-z.
50. *GB/T 1346-2011*; Test Methods for Water Requirement of Normal Consistency, Setting Time and Soundness of the Portland Cement. China Architecture & Building Press: Beijing, China, 2011.
51. Zhang, D.-W.; Zhao, K.-F.; Li, H.; Wang, D.-M.; Wang, L.-L.; Zhang, G.-F. Dispersion properties of fly ash–slag powders under the different environment. *Constr. Build. Mater.* **2021**, *296*, 123649. https://doi.org/10.1016/j.conbuildmat.2021.123649.
52. *ASTM C109/C109M-20a*; Standard Test Method for Compressive Strength of Hydraulic Cement Mortars (Using 2-in. Or [50-mm] Cube Specimens). ASTM International: West Conshohocken, PA, USA, 2016.
53. Yokota, H.; Rokugo, K.; Sakata, N. JSCE Recommendations for design and construction of high performance fiber reinforced cement composites with multiple fine cracks. In *High Performance Fiber Reinforced Cement Composites*; Springer: Tokyo, Japan, 2008; pp. 1–16.
54. Arunothayan, A.R.; Nematollahi, B.; Ranade, R.; Bong, S.H.; Sanjayan, J. Development of 3D-printable ultra-high performance fiber-reinforced concrete for digital construction. *Constr. Build. Mater.* **2020**, *257*, 119546. https://doi.org/10.1016/j.conbuildmat.2020.119546.
55. Lei, D.-Y.; Li, M.-A.; Wang, P.-G.; Guo, L.-P.; Li, Y.; Liu, J.-P.; Zhang, P.; Li, S.-C.; Li, C.-C.; Li, Z.-H.; et al. Design of ultra-high strength, ultra-high ductility cementitious composites (UHS-UHDCC). *Constr. Build. Mater.* **2022**, *322*, 125914. https://doi.org/10.1016/j.conbuildmat.2021.125914.
56. Xu, S.; Yuan, P.; Liu, J.; Pan, Z.; Liu, Z.; Su, Y.; Li, J.; Wu, C. Development and preliminary mix design of ultra-high-performance concrete based on geopolymer. *Constr. Build. Mater.* **2021**, *308*, 125110. https://doi.org/10.1016/j.conbuildmat.2021.125110.
57. Lao, J.-C.; Xu, L.-Y.; Huang, B.-T.; Zhu, J.-X.; Khan, M.; Dai, J.-G. Utilization of sodium carbonate activator in strain-hardening ultra-high-performance geopolymer concrete (SH-UHPGC). *Front. Mater.* **2023**, *10*, 1142237. https://doi.org/10.3389/fmats.2023.1142237.
58. Kanda, T.; Li, V.C. Practical Design Criteria for Saturated Pseudo Strain Hardening Behavior in ECC. *J. Adv. Concr. Technol.* **2006**, *4*, 59–72. https://doi.org/10.3151/jact.4.59.

59. Yu, K.; Wang, Y.; Yu, J.; Xu, S. A strain-hardening cementitious composites with the tensile capacity up to 8%. *Constr. Build. Mater.* **2017**, *137*, 410–419. https://doi.org/10.1016/j.conbuildmat.2017.01.060.
60. Zhang, Z.; Yuvaraj, A.; Di, J.; Qian, S. Matrix design of light weight, high strength, high ductility ECC. *Constr. Build. Mater.* **2019**, *210*, 188–197. https://doi.org/10.1016/j.conbuildmat.2019.03.159.
61. Alrefaei, Y.; Dai, J.-G. Tensile behavior and microstructure of hybrid fiber ambient cured one-part engineered geopolymer composites. *Constr. Build. Mater.* **2018**, *184*, 419–431. https://doi.org/10.1016/j.conbuildmat.2018.07.012.
62. Gollakota, A.R.; Volli, V.; Shu, C.-M. Progressive utilisation prospects of coal fly ash: A review. *Sci. Total. Environ.* **2019**, *672*, 951–989. https://doi.org/10.1016/j.scitotenv.2019.03.337.
63. Shah, S.F.A.; Chen, B.; Oderji, S.Y.; Haque, M.A.; Ahmad, M.R. Improvement of early strength of fly ash-slag based one-part alkali activated mortar. *Constr. Build. Mater.* **2020**, *246*, 118533. https://doi.org/10.1016/j.conbuildmat.2020.118533.
64. Zhao, S.; Xia, M.; Yu, L.; Huang, X.; Jiao, B.; Li, D. Optimization for the preparation of composite geopolymer using response surface methodology and its application in lead-zinc tailings solidification. *Constr. Build. Mater.* **2020**, *266*, 120969. https://doi.org/10.1016/j.conbuildmat.2020.120969.
65. Wang, Y.; Ma, J.; Qing, L.; Liu, L.; Shen, B.; Li, S.; Zhang, Z. Accelerated carbonation pretreatment of municipal solid waste incineration fly ash and its conversion to geopolymer with coal fly ash. *Constr. Build. Mater.* **2023**, *383*, 131363. https://doi.org/10.1016/j.conbuildmat.2023.131363.
66. Lv, Q.; Yu, J.; Ji, F.; Gu, L.; Chen, Y.; Shan, X. Mechanical Property and Microstructure of Fly Ash-Based Geopolymer Activated by Sodium Silicate. *KSCE J. Civ. Eng.* **2021**, *25*, 1765–1777. https://doi.org/10.1007/s12205-021-0025-x.
67. Shi, Y.; Long, G.; Ma, C.; Xie, Y.; He, J. Design and preparation of ultra-high performance concrete with low environmental impact. *J. Clean. Prod.* **2019**, *214*, 633–643. https://doi.org/10.1016/j.jclepro.2018.12.318.
68. Turner, L.K.; Collins, F.G. Carbon dioxide equivalent (CO_2-e) emissions: A comparison between geopolymer and OPC cement concrete. *Constr. Build. Mater.* **2013**, *43*, 125–130. https://doi.org/10.1016/j.conbuildmat.2013.01.023.
69. Yang, T.; Zhang, Z.; Zhang, F.; Gao, Y.; Wu, Q. Chloride and heavy metal binding capacities of hydrotalcite-like phases formed in greener one-part sodium carbonate-activated slag cements. *J. Clean. Prod.* **2020**, *253*, 120047. https://doi.org/10.1016/j.jclepro.2020.120047.
70. Dong, Z.; Tan, H.; Yu, J.; Liu, F. A feasibility study on Engineered cementitious Composites mixed with coarse aggregate. *Constr. Build. Mater.* **2022**, *350*, 128587. https://doi.org/10.1016/j.conbuildmat.2022.128587.
71. Jin, Q.; Li, V.C. Development of lightweight engineered cementitious composite for durability enhancement of tall concrete wind towers. *Cem. Concr. Compos.* **2018**, *96*, 87–94. https://doi.org/10.1016/j.cemconcomp.2018.11.016.